

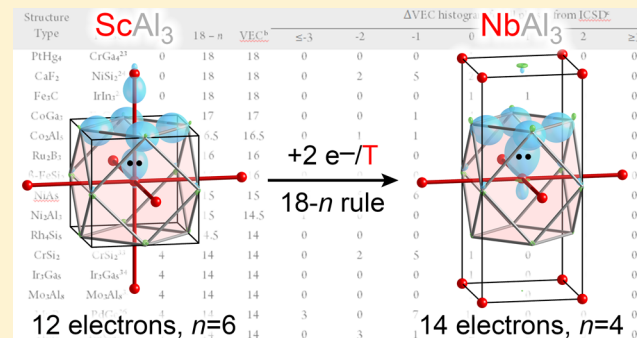
## Generality of the 18-*n* Rule: Intermetallic Structural Chemistry Explained through Isolobal Analogies to Transition Metal Complexes

Vincent J. Yannello and Daniel C. Fredrickson\*

Department of Chemistry, University of Wisconsin–Madison, 1101 University Avenue, Madison, Wisconsin 53706, United States

### S Supporting Information

**ABSTRACT:** Intermetallic phases exhibit a vast structural diversity in which electron count is known to be one controlling factor. However, chemical bonding theory has yet to establish how electron counts and structure are interrelated for the majority of these compounds. Recently, a simple bonding picture for transition metal (T)–main group (E) intermetallics has begun to take shape based on isolobal analogies to molecular T complexes. This bonding picture is summarized in the 18-*n* rule: each T atom in a T–E intermetallic phase will need 18-*n* electrons to achieve a closed-shell 18-electron configuration, where *n* is the number of electron pairs it shares with other T atoms in multicenter interactions isolobal to T–T bonds. In this Article, we illustrate the generality of this rule with a survey over a wide range of T–E phases. First, we illustrate how three structural progressions with changing electron counts can be accounted for, both geometrically and electronically, with the 18-*n* rule: (1) the transition between the fluorite and complex  $\beta$ -FeSi<sub>2</sub> types for TSi<sub>2</sub> phases; (2) the sequence from the marcasite type to the arsenopyrite type and back to the marcasite type for TSb<sub>2</sub> compounds; and (3) the evolution from the AuCu<sub>3</sub> type to the ZrAl<sub>3</sub> and TiAl<sub>3</sub> types for TAi<sub>3</sub> phases. We then turn to a broader survey of the applicability of the 18-*n* rule through a study of the following 34 binary structure types: PtHg<sub>4</sub>, CaF<sub>2</sub> (fluorite), Fe<sub>3</sub>C, CoGa<sub>3</sub>, Co<sub>2</sub>Al<sub>5</sub>, Ru<sub>2</sub>B<sub>3</sub>,  $\beta$ -FeSi<sub>2</sub>, NiAs, Ni<sub>2</sub>Al<sub>3</sub>, Rh<sub>4</sub>Si<sub>5</sub>, CrSi<sub>2</sub>, Ir<sub>3</sub>Ga<sub>5</sub>, Mo<sub>3</sub>Al<sub>8</sub>, MnP, TiSi<sub>2</sub>, Ru<sub>2</sub>Sn<sub>3</sub>, TiAl<sub>3</sub>, MoSi<sub>2</sub>, CoSn, ZrAl<sub>3</sub>, CsCl, FeSi, AuCu<sub>3</sub>, ZrSi<sub>2</sub>, Mn<sub>2</sub>Hg<sub>5</sub>, FeS<sub>2</sub> (*o*P<sub>6</sub>, marcasite), CoAs<sub>3</sub> (skutterudite), PdSn<sub>2</sub>, CoSb<sub>2</sub>, Ir<sub>3</sub>Ge<sub>7</sub>, CuAl<sub>2</sub>, Re<sub>3</sub>Ge<sub>7</sub>, CrP<sub>2</sub>, and Mg<sub>2</sub>Ni. Through these analyses, the 18-*n* rule is established as a framework for interpreting the stability of 341 intermetallic phases and anticipating their properties.



## INTRODUCTION

Intermetallic compounds represent a branch of metallic phases with an immense structural diversity. Their structures often exhibit intriguing geometrical motifs such as multishelled icosahedral clusters,<sup>1</sup> intertwined helices,<sup>2</sup> fragments of simpler crystal structures,<sup>2b,3</sup> and incommensurate modulations,<sup>4</sup> whose rationalization and control remains an important challenge for materials design. One key factor determining the structures of these compounds is electron count. Empirical observations have long traced some of these structures to specific ranges of valence electron concentration.<sup>5</sup> However, bonding schemes allowing us to determine a structure's preferred electron count (without a full quantum mechanical calculation) remain elusive for most compounds.

Progress in developing such schemes for intermetallics has mainly grown out of two simple but powerful ideas: the Mott–Jones and Zintl models. The Mott–Jones model, as has been famously applied to brasses (Cu–Zn phases), views bonding in terms of a gas of free electrons that are only weakly affected by the presence of the ion cores of the atoms.<sup>5a,6</sup> For any given electron count, structures are preferred that allow matching between the atomic positions and the periodicity of the highest occupied plane wave-like states (as occurs when a Fermi surface

in k-space touches the Brillouin zone). In such cases, mixing of these frontier wave functions can create a stabilizing energy gap between occupied standing waves whose maxima lie on the atomic centers and unoccupied waves whose maxima lie between the atoms. This model, of course, assumes virtually complete delocalization of the valence electrons.

The Zintl concept, however, considers a different situation: the formation of compounds between elements with very different electronegativities.<sup>7</sup> Here stable electron counts are achieved via oxidation of the electropositive element by the electronegative one, followed by covalent bonding between the atoms of the electronegative element (or sometimes the less electronegative ones<sup>8</sup>) to satisfy molecular electron-counting schemes, most often the octet rule. At the heart of this picture is the localization of electron pairs into bonds between atoms of the structure, though adepts of Zintl chemistry recognize this as an approximation of a more complex reality.

Both of these models have been very productive in explaining structural chemistry and inspiring the discovery of new compounds. However, they represent only limiting cases in

Received: August 31, 2015

Published: November 19, 2015

the great diversity of intermetallic phases. Indeed, the pursuit of polar intermetallics at the boundaries between these categories has opened new structural realms in the chemistry of metals and alloys.<sup>9</sup> Electronic band gaps or pseudogaps associated with special stability have been identified for many such compounds beyond the Mott–Jones or Zintl domains of applicability,<sup>10</sup> but for most, bonding pictures linking structure and electron count have yet to be drawn.

In this Article, we build a case for a broadly applicable bonding scheme for transition metal-containing intermetallics that are untamed by the Mott–Jones and Zintl pictures. Our initial clues to this scheme were found in the complex structures of  $\text{Fe}_8\text{Al}_{17.4}\text{Si}_{7.6}$ <sup>11</sup> and  $\text{Co}_3\text{Al}_4\text{Si}_2$ .<sup>12</sup> With density functional theory (DFT)-calibrated Hückel calculations, we traced their structural features to the bonding of a common parent phase:  $\text{NiSi}_2$ , which adopts the simple  $\text{CaF}_2$  type.  $\text{NiSi}_2$ 's electronic structure is built from 18-electron configurations on the Ni atoms, which only weakly interact with each other, a scheme that recalls earlier conclusions about 18-electron half-Heusler phases.<sup>10h,n</sup> When substituting Ni with Co or Fe, and some of the Si with Al, this preferred electron count cannot be maintained within the confines of a 1:2 stoichiometry of transition metal (T) and main group (E) atoms. The complex structures of  $\text{Fe}_8\text{Al}_{17.4}\text{Si}_{7.6}$  and  $\text{Co}_3\text{Al}_4\text{Si}_2$  provide avenues for restoring these 18-electron configurations.

These conclusions pointed toward analogies between intermetallics and 18-electron coordination compounds or organometallic complexes. To test this idea, we developed a method for mapping the electronic structures of intermetallics to simple molecular orbital (MO) diagrams, the reversed approximation MO (raMO) approach,<sup>13</sup> effectively allowing for the rapid testing of isolobal analogies between solid-state and molecular structures. With this tool in hand, the importance of 18-electron configurations was revealed in  $\text{CrGa}_4$ ,<sup>13</sup>  $\text{Ir}_3\text{Ge}_7$ -type phases,<sup>13</sup> the carbometalate  $\text{Gd}_{13}\text{Fe}_{10}\text{C}_{13}$ ,<sup>14</sup> and the Nowotny chimney ladder phases.<sup>15</sup>

Over the course of this Article, we demonstrate how these earlier results lay the framework for a general electron counting rule for T-containing intermetallics, the 18-*n* rule. After proposing this rule and its underlying theoretical rationale, we show its usefulness in explaining three structural progressions between intermetallic structure types in terms of T–T bonds forming or breaking in response to changes in the electron count. In addition, we will interpret the stability and T–T connectivity of phases in 34 binary structure types, accounting for the stability of several hundred phases. In the process, the 18-*n* rule will emerge as a means to counting electrons in intermetallics with the same ease as in organometallic compounds. And just as organometallics with unusual electron counts are frequently associated with interesting reactivity, violations to the 18-*n* rule in intermetallics can be expected to have consequences for electronic and magnetic properties.

## ■ EXPERIMENTAL METHODS

**Electronic Structure Calculations.** Bonding analyses applying the reversed approximation Molecular Orbital (raMO) method were performed using a single procedure for a variety of T–E intermetallic phases (listed in the Supporting Information). This procedure began with the geometrical optimization of the structure with GGA-DFT, using the Vienna ab initio Simulation Package (VASP),<sup>16</sup> in which a relaxation of the atomic positions within a fixed unit cell was followed by the release of all structural parameters. Single-point calculations were then performed to obtain band energies and density of states

(DOS) curves, to serve as a basis for the generation of an effective Hückel model for the system. All GGA-DFT calculations were performed in the high precision mode, using the projector augmented wave (PAW) potentials provided with the package<sup>17</sup> and k-point meshes sufficiently fine to converge the total energy to within one millielectronvolt per atom.

The program eHtuner<sup>18</sup> was then used to refine DFT-calibrated Hückel parameters against the GGA-DFT results for use in the raMO analysis, with the simple Hückel calculations themselves being run with YAeHMOP.<sup>19</sup> The basis set employed in these Hückel models included the valence s, p, and d orbitals for transition metals, while most main-group elements were modeled with valence s and p orbitals. For Al, however, we found that including the 3d orbitals led to a substantial improvement in the fits to the DFT results, as can be understood from the observation that the Al d projected DOS near the Fermi energy is generally of comparable magnitude to that of the T p (the final raMO results, however, depend little on whether Al 3d orbitals are used). Following the parametrization, simple Hückel calculations were performed on a supercell of the conventional cell to fold several high-symmetry k points onto the  $\Gamma$  point. The  $\Gamma$ -point Hamiltonian matrix was then extracted and imported into MATLAB, where raMO analysis was performed using in-house functions. Details pertaining to the calculations for each phase are listed in the Supporting Information.

## ■ THE 18-*n* RULE

The central goal of this Article is to establish the following electron counting rule for transition metal (T)–main group (E) intermetallic phases: each T atom in a compound will require 18-*n* electrons to achieve a closed-shell electron count, where *n* is the number of electron pairs that it shares with neighboring T atoms. Additional electrons may be required for bonding between the E atoms (analogous to electrons internal to the ligands in molecular T complexes). In such cases, the overall preferred electron concentration for a compound is expected to be 18-*n+m* electrons per T atom, where *m* is the average number of electrons in E-based orbitals per T atom. Adherence to this rule is expected to lend a phase special stability and possibly a band gap or pseudogap at its Fermi energy ( $E_F$ ), while deviations from this rule point toward a tendency for structural transformations or interesting physical properties arising from a large density of states (DOS) at the  $E_F$ .

To illustrate the chemical meaning of the *n* and *m* parameters, let us consider an example:  $\text{Ir}_3\text{Sn}_7$ , whose adherence to the 18-*n* bonding picture we established previously (Figure 1).<sup>13</sup> In our analysis of this phase, we found that filled 18-electron configurations are present on each of the Ir atoms. However, these closed shells on the Ir atoms are not achieved independently of each other. The Ir atoms occur in pairs, which are linked through shared electron pairs in multicenter functions. These functions have the same symmetry properties as an Ir–Ir  $\sigma$  bond but involve substantial contributions from bridging Sn atoms. We will refer to such functions as *isolobal*<sup>20</sup> T–T bonds, as from the point of view of electron bookkeeping, they can be treated as electron pairs shared between the T atoms.<sup>21</sup> As the T atoms each participate in *n* = 1 shared electron pair, they can achieve 18-electron configurations with only  $18 - 1 = 17$  electrons each.

This number does not, however, correspond to the full valence electron count per Ir atom in the phase; additional electron pairs occur in Sn–Sn  $\sigma$  bonds that are independent of the Ir atoms. Four such bonds occur per formula unit of  $\text{Ir}_3\text{Sn}_7$ , leading to  $m = (4 \times 2)/3 = 1.33$  electrons per Ir. The overall electron count for the phase is then predicted to be  $18 - 1 + 1.33 = 18.33$ , in agreement with that given by the

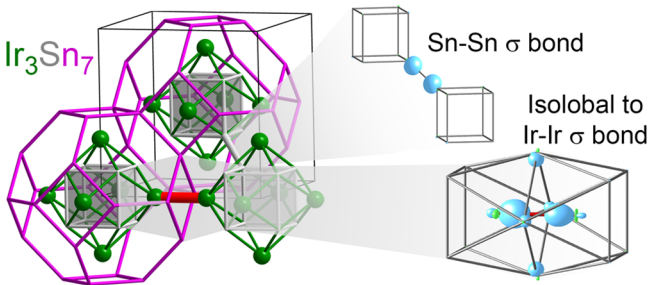


**Figure 1.** The 18-*n* rule illustrated with  $\text{Ir}_3\text{Sn}_7$  ( $\text{Ir}_3\text{Ge}_7$  type). The Ir atoms occur in pairs that are linked through one covalently shared electron pair in a function isolobal to an Ir–Ir  $\sigma$  bond ( $n = 1$ ). Eighteen electron configurations on the Ir atoms can then be achieved with  $18 - 1 = 17$  electrons per Ir. A raMO analysis reveals that  $\text{Ir}_3\text{Sn}_7$  also has Sn–Sn bonds that are noninteracting with the Ir atoms, requiring 1.33 electrons per Ir atom ( $m = 1.33$ ). The optimal valence electron count for the phase is then  $18 - n + m = 18 - 1 + 1.33 = 18.33$  electrons per Ir atom, in agreement with that calculated from the stoichiometry.

compound's formula:  $(9 \times 3 + 4 \times 7)/3 = 18.33$  electrons per Ir. The favorability of this count is confirmed by the presence of a pseudogap at the  $E_F$  for this phase.

In the next sections, we will see how this simple approach to electron counting can make sense of structural progressions between intermetallic phases and provides a context for understanding the stability ranges of 34 binary T–E structure types. A key lens discerning these bonding schemes is provided by the raMO method, which will be illustrated through a series of examples, building from simple to increasingly complex.

## ■ FROM $\text{NiSi}_2$ TO $\beta\text{-FeSi}_2$

Let us begin with one of the simplest 18-electron phases,  $\text{NiSi}_2$  ( $n = 0$ ), and its relationship to the important semiconductor and thermoelectric material  $\beta\text{-FeSi}_2$ .<sup>22</sup>  $\text{NiSi}_2$  crystallizes in the fluorite ( $\text{CaF}_2$ ) structure type, in which the Si atoms build a primitive cubic lattice (gray, Figure 2a) with every other cubic hole being occupied by Ni atoms. This arrangement can alternatively be viewed as a face-centered cubic (fcc) arrangement of vertex-sharing  $\text{Ni@Si}_8$  cubes. A clue to the stability of this arrangement is found in its electronic DOS distribution (Figure 3a). A pseudogap is observed just below the  $E_F$ , a feature that is often associated with a favorable electronic count (this one is shallow compared to others we will see in this Article). The valence electron count of this phase is 18 per Ni atom, suggesting the possibility that the pseudogap coincides with the filling of 18-electron configurations on the Ni atoms. This picture for  $\text{NiSi}_2$  can be tested with the raMO approach.

The raMO approach is based on a reversal of the basis-set approximation at the heart of most MO calculations and electronic structure calculations in general (Figure 4). In a typical MO calculation, simple basis functions are used to reproduce complicated MOs. The raMO method, however, has the goal of creating simple, easily interpretable functions from the fully occupied MOs (or crystal orbitals in an extended solid). In other words, the occupied wave functions are used as a basis set for solving a model bonding problem with simple solutions. The output of the method is a set of raMO functions that give the best reproductions of a given set of target functions possible from the full electronic structure of a compound.<sup>23</sup>

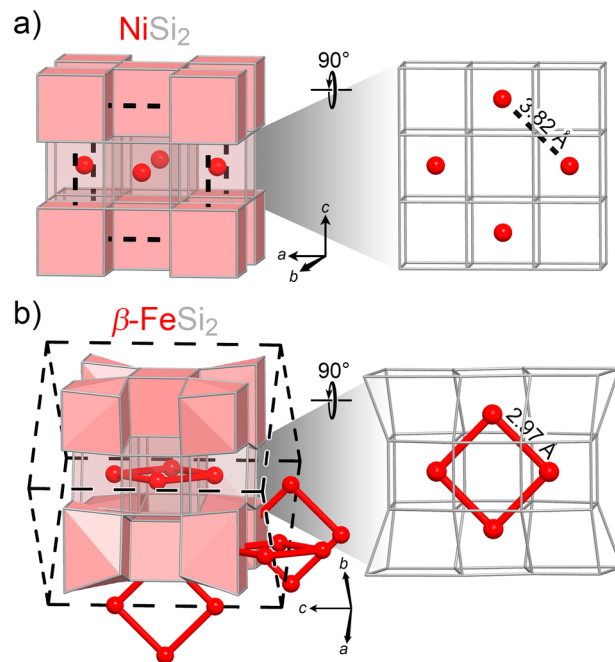


**Figure 2.** Comparison of the crystal structures of (a)  $\text{NiSi}_2$  with 18 valence electrons per T and (b)  $\beta\text{-FeSi}_2$  with 16 electrons per T. In the fluorite-type structure of  $\text{NiSi}_2$ , the T atoms are relatively isolated from each other with a shortest interatomic distance being 3.82 Å. The replacement of Ni with Fe (with a loss of two valence electrons per T atom) leads to the coalescence of the T atoms into squares with significantly shorter T–T distances of 2.97 Å.

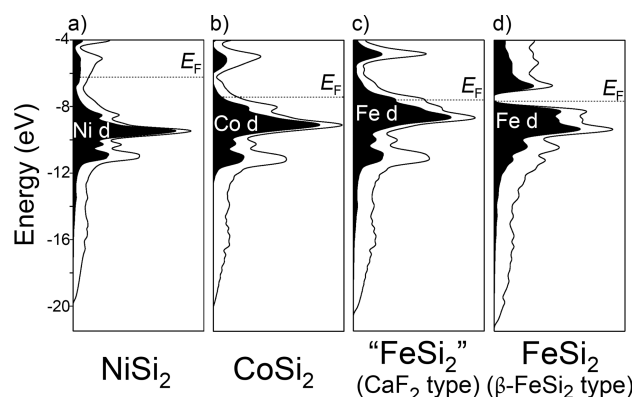


**Figure 3.** GGA-DFT electronic DOS distributions for the fluorite-type phases (a)  $\text{NiSi}_2$ , (b)  $\text{CoSi}_2$ , and (c)  $\text{FeSi}_2$  (hypothetical), as well as (d)  $\beta\text{-FeSi}_2$ . The T d contributions to the DOS distributions are shaded in black.

## MO Method:

$$\psi_{\text{MO}} = \sum c_j \phi_{\text{basis},j}$$

## raMO Method:

$$\phi_{\text{target}} \approx \sum_{j \in \text{occupied states}} c_j \psi_{\text{MO},j}$$

**Figure 4.** Comparison of the relationship between a model basis set (green) and calculated molecular/crystal orbitals (blue) in the raMO and traditional MO methods.

As the stability of  $\text{NiSi}_2$  appears to be correlated with the Ni atoms achieving a filled octadecet, we expect that the electronic structure should contain electron pairs associated with the nodal characters of the Ni atoms' valence 4s, 4p, and 3d orbitals. A simple way to attempt the construction of raMO functions corresponding to these electron pairs is to consider the nine Ni valence orbitals as a target MO diagram, construct a model Hamiltonian in which these are the true eigenfunctions, and use  $\text{NiSi}_2$ 's states below the  $E_F$  as an approximate basis set for calculating eigenvectors (the desired raMOs) for the model Hamiltonian matrix (Figure 5a,b).

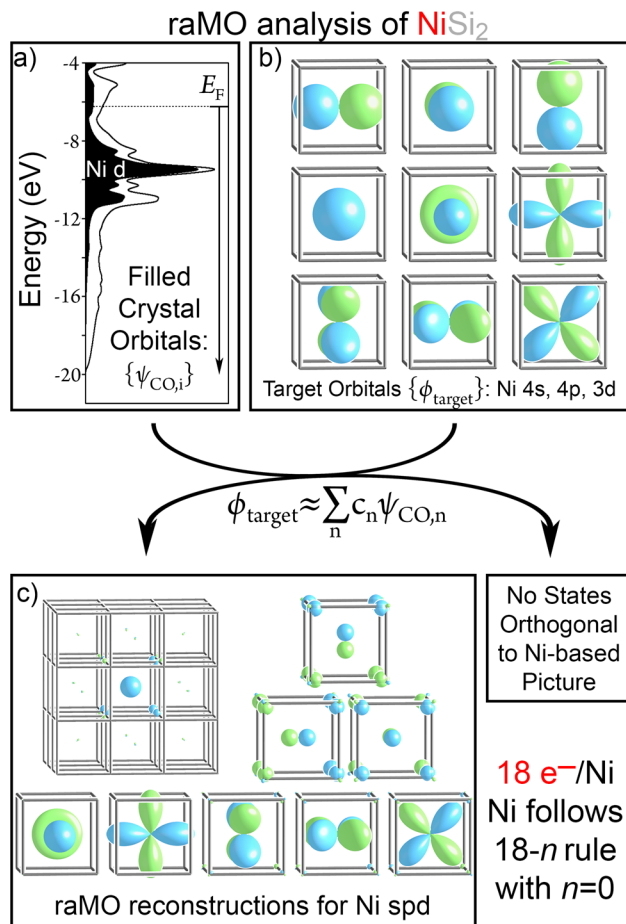


**Figure 5.** The raMO method applied to  $\text{NiSi}_2$ . (a) Occupied crystal orbitals (COs) of  $\text{NiSi}_2$ , represented by the DOS curve below the  $E_F$ . (b) The target Ni s, p, and d orbitals used in the analysis. (c) Reconstructions of the nine valence atomic orbitals of a Ni atom in  $\text{NiSi}_2$ . The 4s orbital-based function is shown in its wider context of the structure to demonstrate its strong localization to the first coordination environment of the Ni atom. For the remaining functions, we focus just on the Ni atom's local environment.

The raMOs that result from this procedure for  $\text{NiSi}_2$  (Figure 5c) nicely show the same nodal properties as the original atomic orbitals of the Ni atom but are augmented by in-phase contributions from the neighboring Si atoms that introduce Ni–Si and Si–Si bonding, especially in the Ni 4s- and 4p-centered functions. The raMO functions are strongly localized to the Ni atom plus its first coordination environment, as is shown explicitly for the Ni 4s-based raMO. As these functions are all built from linear combinations of occupied crystal orbitals, they each contain a pair of electrons, supporting the

hypothesis that the Ni atoms have closed-shell 18-electron configurations.

Our assignment of all electrons to essentially independent Ni centers is affirmed by a full raMO analysis of the phase in which the crystal orbitals of the Ni sublattice are used as target functions. This analysis is able to account for all of the occupied wave functions for  $\text{NiSi}_2$ , meaning that there are no electrons left over. As the Ni atoms appear independent from each other (with no Ni–Ni interactions apparent in the raMO functions), these results can be summarized with the conclusion that  $\text{NiSi}_2$  follows the 18-*n* rule in the simplest way, with *n* = 0 and *m* = 0.

Having confirmed this bonding picture for  $\text{NiSi}_2$ , one might wonder how strict this preference is for 18-electrons per Ni. For example, how would the structure respond to substitutions that pull electrons out of these closed-shell configurations? Replacing Ni with Co brings us to the 17 electron phase  $\text{CoSi}_2$ , which also adopts the fluorite type. The  $E_F$  now lies below the pseudogap (Figure 3b), confirming that it is electron-poor relative to the ideal. However, this deficiency appears to be tolerated, which can be understood with an raMO analysis of  $\text{CoSi}_2$  (see Supporting Information), which shows only small changes relative to the results for  $\text{NiSi}_2$ .

Moving to  $\text{FeSi}_2$  (16 electrons per T), however, has more serious consequences. If  $\text{FeSi}_2$  were to maintain the fluorite type as  $\text{NiSi}_2$  and  $\text{CoSi}_2$  do, its  $E_F$  would lie far below the 18-electron pseudogap in a dense set of Fe d-rich states (Figure 3c). This would be a prime setup for magnetic ordering, but instead a structural response is taken.  $\beta\text{-FeSi}_2$  represents a distorted superstructure of the fluorite type in which the Fe atoms move away from the  $\text{Si}_8$  cube centers to form squares of Fe atoms with Fe–Fe distances of 2.97 Å (Figure 2b). The effectiveness of this structural rearrangement at preventing the electronic instability predicted for  $\text{FeSi}_2$  in the fluorite type is evident in its electrical properties: it is a narrow-bandgap semiconductor with a band gap of ca. 0.9 eV,<sup>22c,24</sup> as is qualitatively confirmed by its DFT DOS distribution (Figure 3d).

The band gap in  $\beta\text{-FeSi}_2$  has been the subject of several previous electronic structure studies, which have attributed the opening of this gap to hybridization between Si p and Fe d orbitals.<sup>25</sup> This form of p–d hybridization mechanism is commonly evoked for T–E intermetallics, and nicely explains the DOS features observed above and below the  $E_F$  for these compounds. It does not, however, provide an explanation for which electron count a band gap or pseudogap should occur for any given phase, e.g. why the fluorite type shows a DOS minimum near 18-electrons per T atom, while in  $\beta\text{-FeSi}_2$  it occurs at 16 electrons per T.

Such a connection between structure and electron count can be found in the 18-*n* rule. To see this, we perform an raMO analysis on  $\beta\text{-FeSi}_2$  using the s, p, and d valence orbitals of one of its Fe atoms as target states. The results reveal strong similarities to those generated for  $\text{NiSi}_2$  (see the Supporting Information for the full set of nine functions), with some key differences. Figure 6a shows the Ni atom's  $p_x$  and  $p_y$  raMOs in an expanded environment, to include the four neighboring Ni atoms. As we saw before, no contributions from the neighboring Ni atoms appear in these states, indicating no bonding interactions between Ni atoms. Placing the Fe atom's  $p_x$  and  $p_y$  raMOs alongside those of the Ni atom makes the distortion's effect clear. Bonding interactions with the two close Fe contacts are prominent in both raMOs, with similar

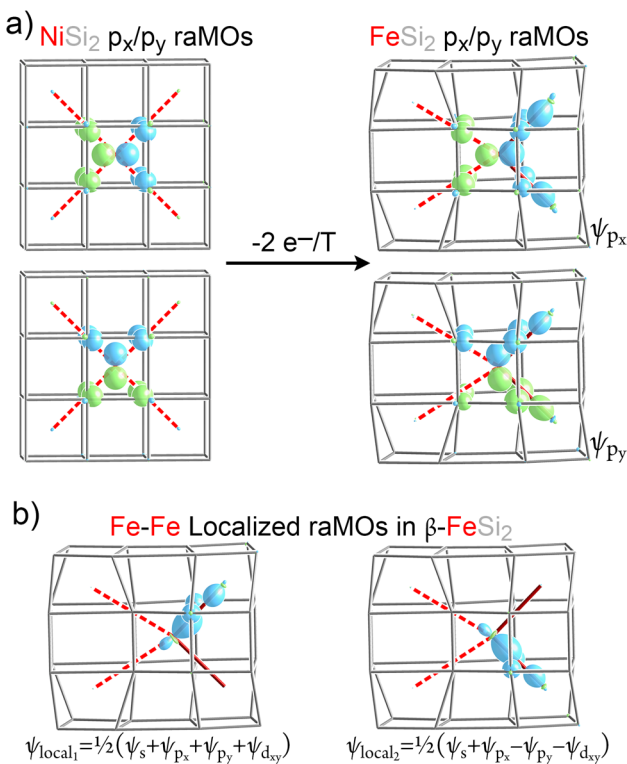


**Figure 6.** Creation of isolobal Fe–Fe bonds in  $\beta\text{-FeSi}_2$  to accommodate a lower electron count. (a) Bonding components from neighboring T atoms appear in the raMO reproductions of the T valence  $p_x$  and  $p_y$  orbitals upon moving from  $\text{NiSi}_2$  to  $\beta\text{-FeSi}_2$ . (b) Linear combinations of the raMO functions creating individual isolobal Fe–Fe bonds.

contributions seen in the  $d_{xy}$  and s raMOs as well (see Supporting Information).

It is possible to further localize these bonding interactions: linear combinations of the s,  $p_x$ ,  $p_y$ , and  $d_{xy}$  raMOs create four

$sp^2$  hybrid orbitals in a square planar arrangement, two of which are Fe–Fe bonding, the other two being lone pairs in terms of Fe–Fe connectivity (Figure 6b). The resulting bonding functions show strong multicenter character with Fe–Fe overlap being substantially strengthened by bonding contributions from bridging Si atoms. As the functions show the same nodal character as traditional  $\sigma$  bonds along the Fe–Fe contacts, they can be described as isolobal Fe–Fe single bonds, each containing a covalently shared electron pair. With each Fe atom having two such bonds ( $n = 2$ ), 18-electron counts can be achieved with only 16 electrons per Fe. This viewpoint is able to account for all of the occupied wave functions, allowing us to conclude that  $\text{FeSi}_2$  follows the 18- $n$  rule, with  $n = 2$  and  $m = 0$ .

The structural distortion on going from  $\text{NiSi}_2$  to  $\beta\text{-FeSi}_2$  is thus easily rationalized as a response to the loss of two electrons around each T atom. If  $\text{FeSi}_2$  were to remain in the fluorite type, each Fe would be deficient by two electrons relative to an 18-electron count. Upon shortening two of the Fe–Fe contacts at each Fe atom, two new bonds form, allowing it to achieve an 18-electron count by the sharing of electrons with each of its two neighbors.  $\text{CoSi}_2$ , with 17 electrons per T, is a sort of middle ground, where forming either the fluorite type or the  $\beta\text{-FeSi}_2$  type would result in violating the 18- $n$  rule. One possible solution to this problem is the dimerization of Co atoms in  $\text{CoSi}_2$ . This change would allow  $\text{CoSi}_2$  to follow the 18- $n$  rule without the need for large distortions. As it appears that the  $\text{CoSi}_2$  structure has not yet been refined against single-crystal data,<sup>26</sup> it may be interesting to reinvestigate its structure, especially at low temperatures where a metal–insulator transition involving Co dimerization could take place.

## ■ FROM MARCASITE TO ARSENOPYRITE AND BACK

In the  $\text{TSi}_2$  series of the last section, all valence electrons in the phases could be assigned to the T centers. Let's move up one step in complexity to a progression of compounds in which additional electrons are found outside the T units: antimonides

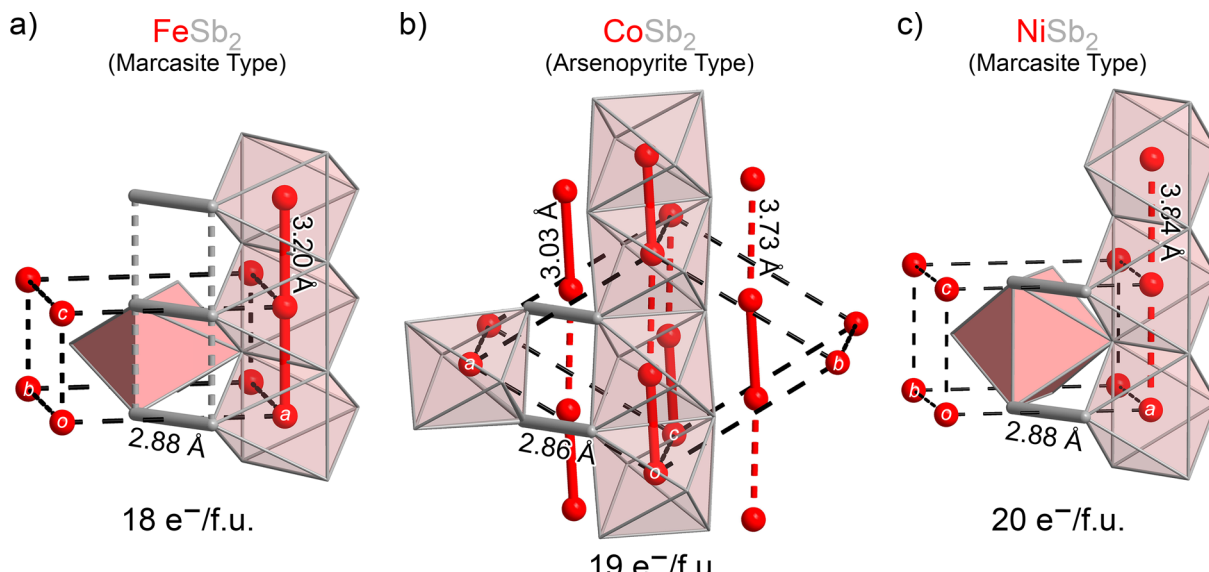


**Figure 7.** Changes in T–T connectivity in marcasite and arsenopyrite  $\text{TSb}_2$  phases with changes in valence electron count. (a) The marcasite structure of  $\text{FeSb}_2$  (18-electrons per formula unit), whose Fe atoms are arranged in linear chains. (b) The arsenopyrite structure of  $\text{CoSb}_2$  (19 electrons per formula unit), where the distances within the corresponding T chains alternate between relatively long and short. (c) The marcasite-type  $\text{NiSb}_2$  (20 electrons per formula unit) in which no short T–T contacts occur.

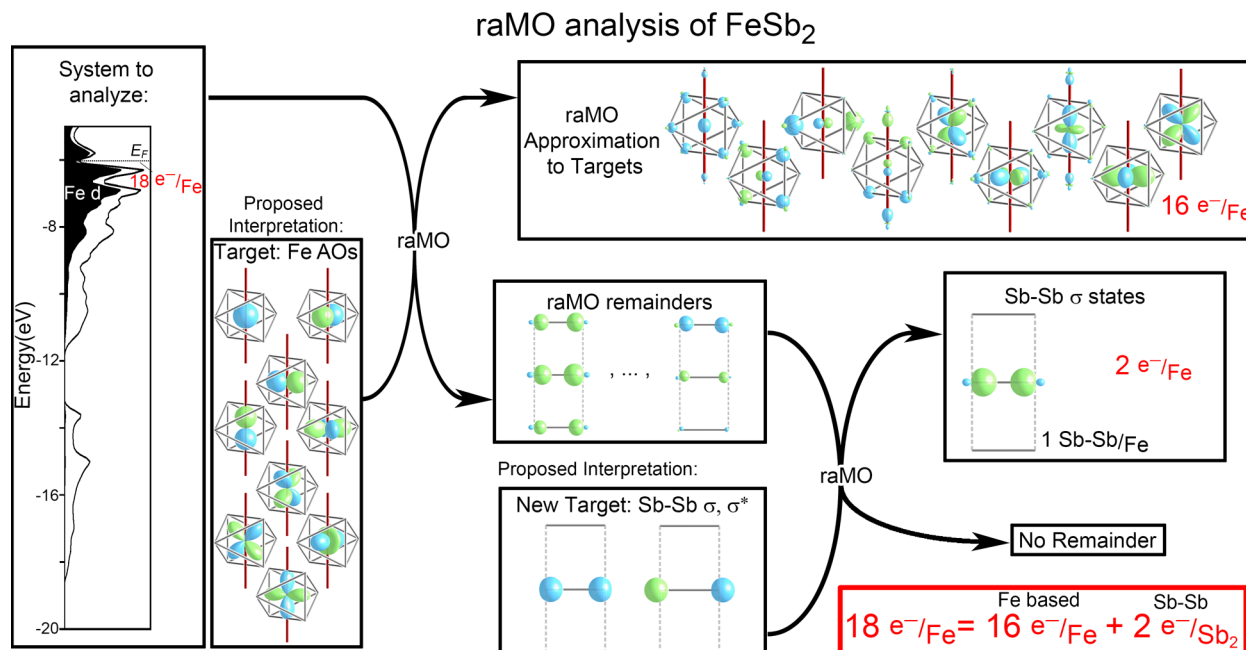


**Figure 8.** A multistep raMO analysis on FeSb<sub>2</sub>. In the first raMO step, the occupied crystal orbitals of FeSb<sub>2</sub> are first used to reproduce the s, p, and d valence atomic orbitals (AOs) of the Fe atoms, leading to a set of raMOs that reconstruct the Fe valence orbitals and a set of remainder functions that are orthogonal to the Fe-centered functions. The remainder functions are then used in a second raMO step with the  $\sigma$  and  $\sigma^*$  functions of the Sb dimers as targets. This step yields a set of raMOs with Sb–Sb  $\sigma$  character and no remainder states. The electronic structure is then resolved into 18- $n$  ( $n = 2$ ) configurations on the Fe atoms, and two electrons per FeSb<sub>2</sub> formula unit in Sb–Sb bonds. This breakdown accounts for the observed electron count of 18 per Fe atom. For clarity, the raMOs depicted for the Fe and Sb–Sb  $\sigma$  are derived using targets located on a single Fe atom or an Sb dimer.

adopting the marcasite and arsenopyrite types.<sup>27</sup> These TSb<sub>2</sub> structures are composed of columns of edge-sharing T@Sb<sub>6</sub> octahedra running along the *c* direction, which are cross-linked through shared corners and Sb–Sb bonds (Figure 7). The columns of octahedra create chains of T atoms, which exhibit T–T distances that are short (FeSb<sub>2</sub>, marcasite type), long (NiSb<sub>2</sub>, marcasite type), or alternating between long and short (CoSb<sub>2</sub>, arsenopyrite type). The T–T elongation corresponds to an expansion of the structure along the chain direction that, from the viewpoint of atomic size, seems counterintuitive: atoms of Co and Ni are slightly smaller than those of Fe, while their incorporation leads to the expansion of the structure along *c*. Instead, an electronic origin is more likely, perhaps reminiscent of the Peierls distortions of one-dimensional metallic systems.<sup>28</sup>

These phases have been the subject of numerous theoretical investigations, which have led to some disagreement about the nature of the T–T interactions along these chains. First-principles calculations on these compounds have mainly focused on reproducing their relative energies and physical properties.<sup>29</sup> In contrast, the most-cited bonding ideas for these phases are derived from qualitative tight-binding considerations.<sup>30</sup> Here, the classic d t<sub>2g</sub>–e<sub>g</sub> splitting of the T d orbitals in an octahedral T environment is used to explain the stability of a T d<sup>6</sup> electron count, as in NiSb<sub>2</sub> where Ni is assigned the oxidation state of 4+ to balance the charge of the Sb atoms, which appear as Sb<sub>2</sub><sup>4-</sup> anions. The structural changes upon moving to a d<sup>5</sup> or d<sup>4</sup> configuration, as in CoSb<sub>2</sub> or FeSb<sub>2</sub>, serve to split the t<sub>2g</sub> orbitals further. Two different origins to these secondary splittings have been proposed: Hulliger and Mooser<sup>30a</sup> attribute them to the formation of T–T bonds, while Goodenough<sup>30c</sup> (and others subsequently<sup>30b,d-g</sup>) trace

them to the tuning of T–E antibonding interactions, with no T–T interactions being necessary.

In the following, we will see how the 18- $n$  rule allows some reconciliation of these models, where the distinction between T–E and T–T interactions is blurred in isolobal T–T bonding. We begin by examining FeSb<sub>2</sub> (Figure 7a), which forms the marcasite type with the T–T contacts being uniformly short (3.20 Å experimentally, 3.17 Å in the GGA-DFT optimized structure). While a bonding analysis of this compound would typically start with an assignment of electrons to the Sb<sub>2</sub> dumbbells following the Zintl concept, the 18- $n$  rule directs us to first investigate the electron configurations on the Fe atoms. A raMO analysis of the single symmetry-distinct Fe site proceeds just as for the TSi<sub>2</sub> compounds of the last section, using the Fe 4s, 4p, and 3d orbitals as targets. The resulting raMOs (Figure 8) show electron pairs associated with each Fe valence orbital; the Fe atom has achieved an 18-electron configuration.

The raMOs also provide insights into the interactions along the Fe–Fe chain. Those raMOs oriented for  $\sigma$  interactions along the chain (the s, p<sub>z</sub>, and d<sub>z<sup>2</sup></sub>) show significant in-phase contributions from the neighboring Fe atoms. Linear combinations of these states can be taken to generate two isolobal Fe–Fe bonds per Fe atom with one additional nonbonding orbital resulting (Figure 9). In terms of the 18- $n$  rule, FeSb<sub>2</sub> can then be assigned as  $n = 2$ .

Such an assignment, however, accounts for only 18 – 2 = 16 electrons per Fe, while the formula unit indicates 18-electrons per Fe. The presence of Sb<sub>2</sub> dimers (Sb–Sb distance: 2.88 Å) would suggest that Sb–Sb bonds are likely places to accommodate the remaining two electrons per Fe atom. This possibility can be explored through a raMO remainder analysis.

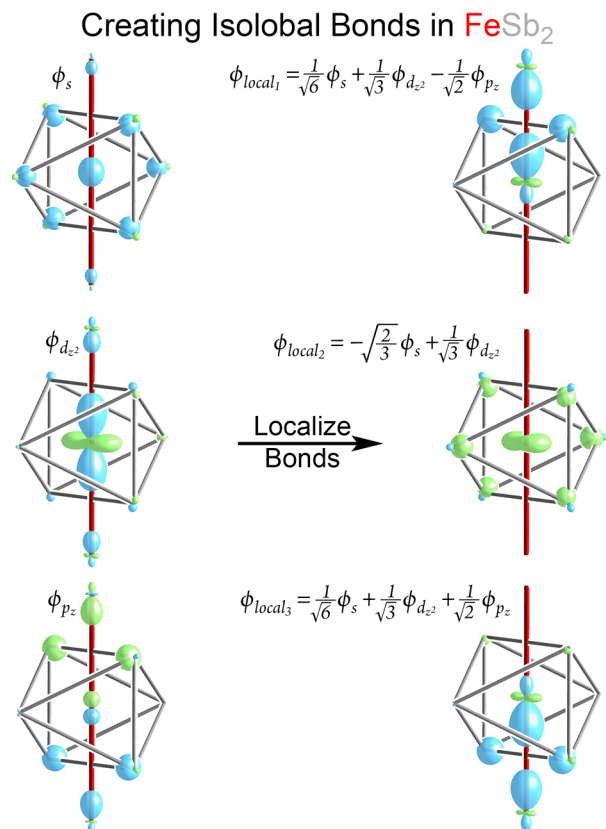


**Figure 9.** Localization of the Fe raMOs in  $\text{FeSb}_2$ , resulting in one lone pair (in terms of Fe–Fe interactions) and two Fe–Fe isolobal bonds.

We first perform an raMO analysis using the crystal orbitals of the Fe sublattice as target functions. This procedure results in two types of raMO functions: those that reproduce Fe-based states, and a set of remainder functions that are orthogonal to the Fe-based raMOs (Figure 8). These orbitals bonding subsystems orthogonal to the target orbitals. A second raMO analysis can be performed on these remainder functions using the lowest two  $\text{Sb}_2$  MOs (with  $\sigma$  and  $\sigma^*$  character) as target orbitals. The results are shown in Figure 8. As is seen, only the state corresponding to a  $\text{Sb}$ – $\text{Sb}$   $\sigma$  bond is reproduced, with no  $\sigma^*$  character being found. In fact, all remainder functions are completely accounted for with  $\sigma$  bonds along the  $\text{Sb}$  dimers.

Note that one requirement for this bonding scheme is that the energy gaps for the filling of the 18-electron configurations on the Fe atoms and the  $\text{Sb}$ – $\text{Sb}$   $\sigma$  bonds should line up at the Fermi energy. That this alignment occurs is affirmed not only by the clarity of the raMO results but also by the presence of a pseudogap at the  $E_F$  for  $\text{FeSb}_2$  (see the DOS distribution in Figure 8).

We thus arrive at a simple breakdown of  $\text{FeSb}_2$ 's valence electron count of 18 per Fe: 16 electrons per Fe serve to provide closed-shell configurations on the Fe atoms, while two electrons per Fe are necessary for the  $\sigma$  bonds in the  $\text{Sb}_2$  dimers. This assignment follows the generalized 18- $n$  rule where the overall electron count of a phase should correspond to  $18 - n + m$ , with  $n = 2$  and  $m = 2$ .

From this viewpoint, we can now easily explain how the system responds to the addition of electrons. On replacing Fe with Co, the electron count is changed from 18 to 19 electrons per T atom. Assuming that the  $\text{Sb}$ – $\text{Sb}$  interactions are left intact (the  $\text{Sb}$ – $\text{Sb}$  distances are essentially unchanged relative

to those of  $\text{FeSb}_2$  at 2.86 Å) so that  $m$  remains equal to 2, there would be 17 electrons left for the Co-centered states. Only a single isolobal Co–Co bond would be necessary for a filled 18-electron configuration, while the marcasite type offers two: a prime setup for a structural transformation.

The structure of  $\text{CoSb}_2$ , in fact, represents a distortion away from the marcasite type to form the arsenopyrite type (Figure 7b). The main effect of this transformation (aside from the reassignment of the cell vectors to create a supercell) is in the Co–Co contacts along the chains of edge-sharing octahedra: one contact of each Co is kept short at 3.03 Å, while the other is lengthened to 3.73 Å. The resulting bond length alternation is consistent with a transition from  $n = 2$  for  $\text{FeSb}_2$  to  $n = 1$  for  $\text{CoSb}_2$ . This picture is confirmed with raMO analysis (Figure 10). While in  $\text{FeSb}_2$  two Fe–Fe isolobal bonds are obtained,

### Localized T–T Bonds in $\text{TSb}_2$ Phases

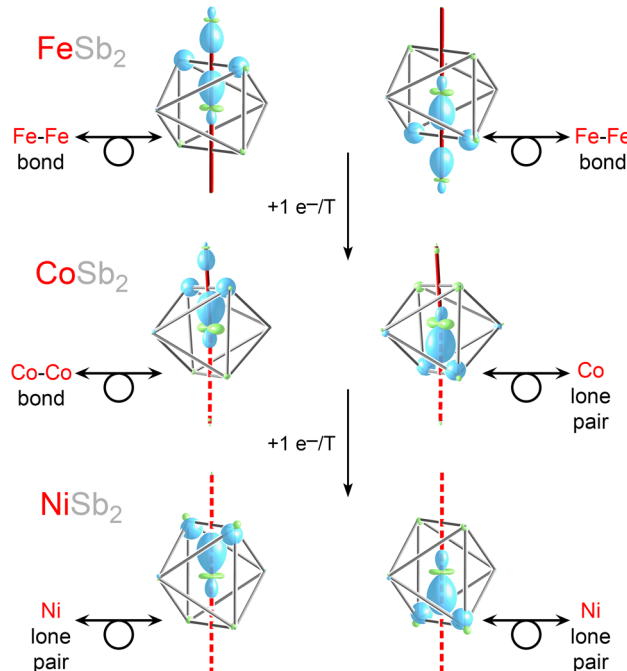


**Figure 10.** Localized raMOs for  $\text{FeSb}_2$ ,  $\text{CoSb}_2$ , and  $\text{NiSb}_2$ . As electrons are added, isolobal T–T bonds become isolobal T lone pairs.

only one of the corresponding functions in  $\text{CoSb}_2$  shows Co–Co bonding. The other function retains the Co–Sb bonding of the original in  $\text{FeSb}_2$  but has no significant component from its Co neighbors. In terms of T–T connectivity, this function is isolobal to a Co lone pair (Figure 10) rather than a Co–Co bond.

Overall, then, the change from the marcasite  $\text{FeSb}_2$  to the arsenopyrite  $\text{CoSb}_2$  corresponds to the cleavage of one T–T bond with the addition of one electron per T atom. The addition of a second electron per T on going to  $\text{NiSb}_2$  might be expected then to involve the breaking of the remaining T–T bond in the arsenopyrite structure. In fact,  $\text{NiSb}_2$  represents a return to the marcasite type (Figure 7c) but now with an elongated  $c$  axis that creates a much longer T–T contact of 3.84 Å. The largely unchanged Sb–Sb contact is maintained at 2.88 Å, supporting the conclusion that the new electron has gone to the Ni center. An raMO analysis verifies this expectation: the analogous linear combinations of the Ni raMOs to the Fe–Fe

or Co–Co isolobal bonds show no significant contributions from the neighboring Ni atoms (Figure 10).

In summary, the structural changes seen through the marcasite–arsenopyrite transitions can be explained in terms of electron counts. Having either 18-electrons per T (e.g., FeSb<sub>2</sub>) or 20 electrons per T (e.g., NiSb<sub>2</sub>) can be accommodated in the marcasite type by having  $n = 2$  or  $n = 0$ , respectively, (with  $m = 2$  arising from the bonds in the Sb dimers). Having an intermediate electron count of 19 electrons per T (as in CoSb<sub>2</sub>) requires a Peierls-like pairing of the T atoms that sets  $n$  to 1. These expectations are mirrored closely by the binary marcasite and arsenopyrite phases in the Inorganic Crystal Structure Database<sup>31</sup> (as we will see in more detail below). The majority of the marcasite phases exhibit electron counts of 18 or 20 per T atom, while all 23 binary arsenopyrite phases included in the database have the predicted 19 electrons per T.

## ■ FROM ScAl<sub>3</sub> TO ZrAl<sub>3</sub> TO NbAl<sub>3</sub>

So far, we have used the 18- $n$  bonding scheme to explain small motions of T atoms in terms of the formation or cleavage of T–T isolobal bonds. Can the same ideas be used to explain larger scale rearrangements in intermetallic structures? One opportunity to explore this possibility is given by a series of TE<sub>3</sub> phases that adopt ordered variants of the fcc structure. Three ordering patterns are typically observed in these compounds, corresponding to the AuCu<sub>3</sub>, ZrAl<sub>3</sub>, and TiAl<sub>3</sub> structure types (Figure 11).

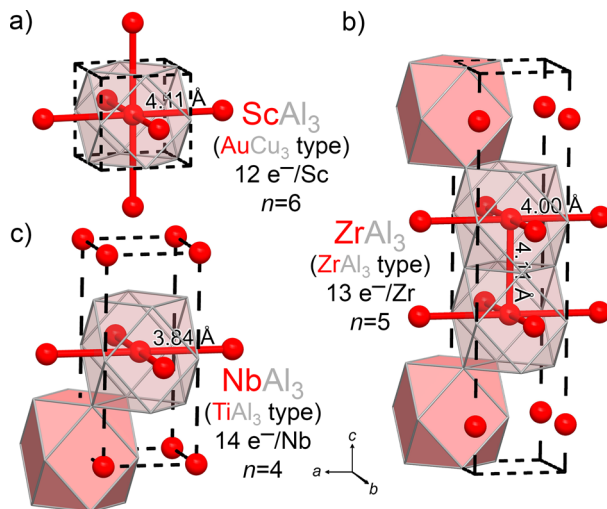


**Figure 11.** Structural progression in TA<sub>3</sub> phases with changes in electron count. (a) The ScAl<sub>3</sub> structure, a representative of the AuCu<sub>3</sub> type (observed at 12 electrons per T) (b) The ZrAl<sub>3</sub> type (observed at 13 electrons per T). (c) The TiAl<sub>3</sub> type (observed at 13–14 electrons per T), exemplified by NbAl<sub>3</sub>.

All three structures are built from E<sub>12</sub> cuboctahedra containing T atoms, with the differences being in how their T@E<sub>12</sub> units are arranged. In the AuCu<sub>3</sub> type, they are arrayed into a primitive cubic fashion through shared square faces. Across each of the six square faces, the central T atom has a relatively distant T neighbor (4.11 Å in ScAl<sub>3</sub>). In the TiAl<sub>3</sub> type, every other layer of T atoms perpendicular to *c* is shifted by a (1/2, 1/2, 0) translation leading to a doubling of the unit cell and a reduction of the T–T connectivity from a primitive cubic framework to a series of parallel square nets. The ZrAl<sub>3</sub>

type represents an intermediate step in which the shifts occur every two T atom layers, leading to each T atom having five T neighbors in a square pyramidal arrangement.

These structures have been the subject of several theoretical investigations aimed at clarifying the role electron concentration plays in their structural preferences.<sup>10a,32</sup> The AuCu<sub>3</sub> and ZrAl<sub>3</sub> types are only adopted when the electron count is 12 or 13 electrons per T, respectively, while the TiAl<sub>3</sub> type can form with either 13 or 14 electrons per T. These preferred electron counts have been previously understood in the context of the DOS distributions (Figure 12). The DOS curves for

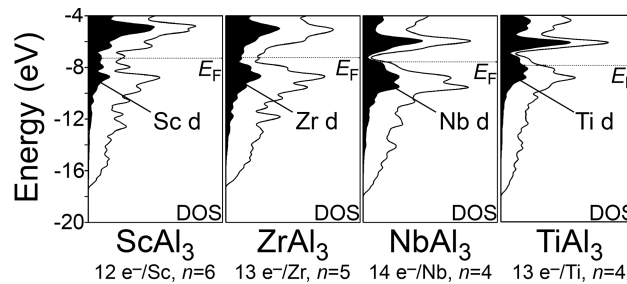


**Figure 12.** GGA-DFT DOS distributions calculated for ScAl<sub>3</sub>, ZrAl<sub>3</sub>, NbAl<sub>3</sub>, and TiAl<sub>3</sub>. The contributions from functions of T d character are shaded in black.

ScAl<sub>3</sub> (AuCu<sub>3</sub> type), ZrAl<sub>3</sub> (ZrAl<sub>3</sub> type), and NbAl<sub>3</sub> (TiAl<sub>3</sub> type) show pseudogaps at the Fermi energies, indicating that a favorable electron count has been achieved. Such DOS features predict that the ideal electron counts for the ScAl<sub>3</sub>, ZrAl<sub>3</sub>, and TiAl<sub>3</sub> types are 12, 13, and 14 per T atom, respectively. Curiously the Fermi energy of TiAl<sub>3</sub>, the archetype of the TiAl<sub>3</sub> type, falls below this pseudogap; its electron count of 13 per T atom thus appears to represent a tolerance for nonideal values rather than a preferred count.

One explanation for the preferred electron counts of AuCu<sub>3</sub>- and TiAl<sub>3</sub>-type aluminides was developed by Condron et al.<sup>10a,32</sup> They began with extending Wade's rules to the aluminum sublattices of these structures and then considered how the atomic orbitals of the T atoms would be affected by interactions with the Al atoms. Through this approach, the ideal counts of 12 and 14 were obtained for the AuCu<sub>3</sub> and TiAl<sub>3</sub> types, respectively. The additional electrons accommodated on going from the AuCu<sub>3</sub> type to the TiAl<sub>3</sub> type is elegantly accommodated by the replacement of octahedral cages of aluminum with square pyramids.

Through raMO analyses on these compounds, we have found that the 18- $n$  bonding scheme offers another way of understanding these trends. Let us start with the simplest of these structures, the AuCu<sub>3</sub> type as is adopted by ScAl<sub>3</sub>. raMO reconstructions of the Sc atom's nine valence atomic orbitals (Figure 13) reveal that each is associated with an electron pair. Substantial contributions from the neighboring aluminum atoms are seen, indicating a strong covalency that can be expected from the relative electronegativities of Sc (1.36) and Al (1.61). In addition, six of the nine raMO functions (those for the *s*, p<sub>x</sub>, p<sub>y</sub>, p<sub>z</sub>, d<sub>z<sup>2</sup></sub>, and d<sub>x<sup>2</sup>-y<sup>2</sup></sub> orbitals) exhibit in-phase contributions from the neighboring Sc atoms. This selection of atomic orbitals is just the right combination to create sp<sup>3</sup>d<sup>2</sup> hybrids pointing toward the corners of an octahedron. Taking the necessary linear combinations yields six Al-supported Sc–Sc bonds (Figure 14a). The preferred electron count of 12 for

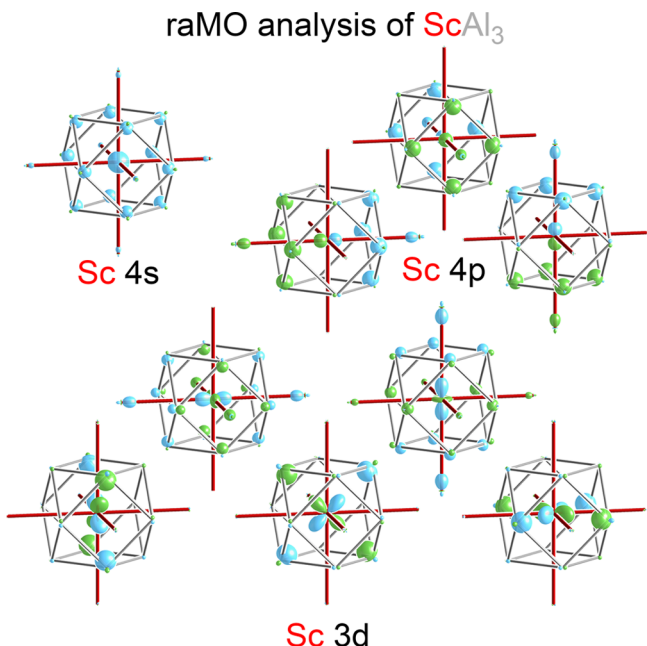


**Figure 13.** raMO reconstructions of the valence atomic orbitals for a Sc atom in  $\text{ScAl}_3$ . The nodal character of all nine atomic orbitals are reproduced, indicating that each is associated with an electron pair.

this structure can thus be simply interpreted as following the  $18-n$  rule with  $n = 6$ .

Similar raMO analyses also trace the structures of  $\text{ZrAl}_3$  and  $\text{NbAl}_3$  to the  $18-n$  bonding scheme. In Figure 14b–c, we focus on the localized functions corresponding to those of  $\text{ScAl}_3$  (the full raMO results can be found in the Supporting Information). On going from  $\text{ScAl}_3$  (12 electrons per Sc) to  $\text{ZrAl}_3$  (13 electrons per Zr), an extra electron per T atom is introduced that must be accommodated by the structure. The new T atom arrangement in the  $\text{ZrAl}_3$  type reduces the T–T contacts around each T atom from 6 to 5, making the preferred  $18-n$  count go up from 12 to 13. Indeed, the six isolobal T–T bonds identified in the localized raMOs of  $\text{ScAl}_3$  now consist of five isolobal bonding functions and one isolobal lone pair (Figure 14b). Moving to  $\text{NbAl}_3$  ( $\text{TiAl}_3$  type) adds another electron per T, which further reduces the number of T–T contacts to four, with another T–T isolobal bond being replaced with an isolobal lone pair (Figure 14c).<sup>33</sup>

The preferences of the  $\text{AuCu}_3$ ,  $\text{ZrAl}_3$ , and  $\text{TiAl}_3$  types for 12, 13, and 14 electrons, respectively, thus have straightforward interpretations in terms of the  $18-n$  rule. One question left unresolved, however, is why  $\text{TiAl}_3$  with 13 electrons per T atom adopts the  $\text{TiAl}_3$  type over the  $\text{ZrAl}_3$  type, which seems preferable for this electron count. One explanation is suggested by a raMO analysis of  $\text{TiAl}_3$ . In it, the majority of the raMO reconstructions of the T valence orbitals are qualitatively very similar to those for  $\text{NbAl}_3$ , showing four interactions isolobal to T–T  $\sigma$  bonds along the 4 T–T contacts. The raMO reconstructions of the T  $d_{xz}$  and  $d_{yz}$  orbitals, however, do show small changes indicative of new bonding (Figure 15). While in  $\text{NbAl}_3$ , no noticeable density is found for these functions on the neighboring Nb atoms, those of  $\text{TiAl}_3$  bear small in-phase d orbitals on the Ti neighbors bonding in a  $\pi$  fashion. Removing one electron per T on going from  $\text{NbAl}_3$  to  $\text{TiAl}_3$  thus corresponds to the depopulation of T–T d-based  $\pi^*$  levels, leading to some net T–T  $\pi$  bonding.

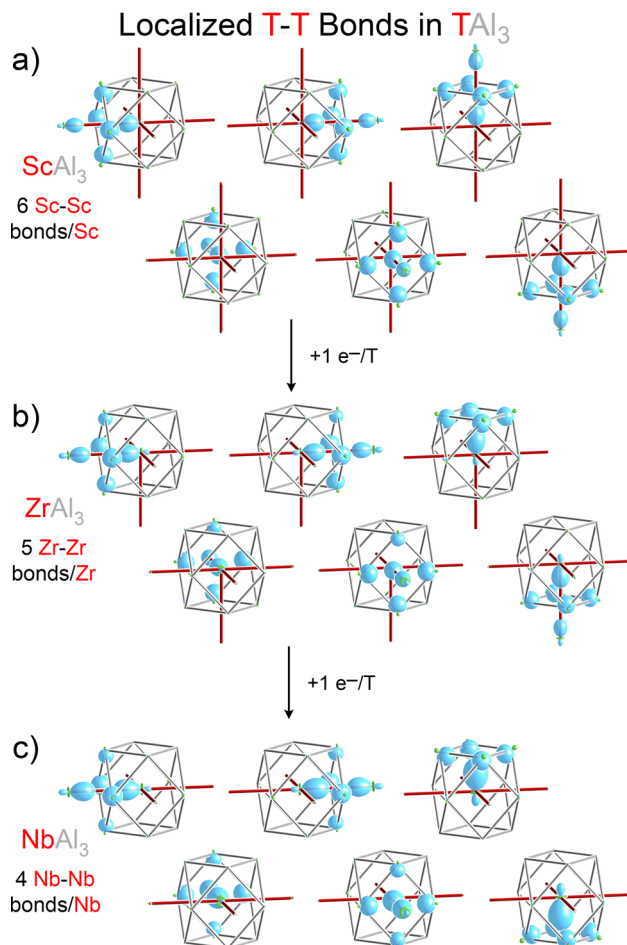


**Figure 14.** Localized functions created from the  $\text{sp}^3\text{d}^2$  hybridization of raMO reconstructions of a T atom's valence orbitals in (a)  $\text{ScAl}_3$ , (b)  $\text{ZrAl}_3$ , and (c)  $\text{NbAl}_3$ . Note that as the electron count is increased, some T–T bonding functions become T–T nonbonding.

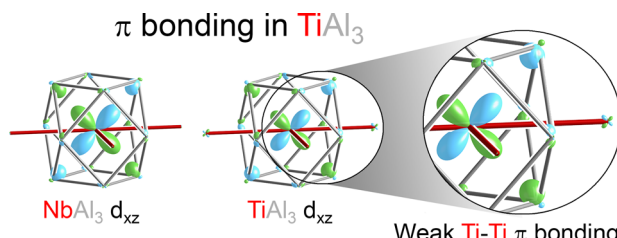


**Figure 15.**  $\pi$  interactions compensating for  $\text{TiAl}_3$  being one electron per T atom short of the count predicted by the  $18-n$  rule.

Similar T–T  $\pi$  bonding was found in our earlier analyses of  $\text{Co}_3\text{Al}_4\text{Si}_2$ <sup>12</sup> and  $\text{Gd}_{13}\text{Fe}_{10}\text{C}_{13}$ <sup>14</sup> where they again play the role of allowing filled 18-electron configurations to be achieved when there are insufficient  $\sigma$  bonds for the number of electrons present. The use of  $\pi$  bonding here is reminiscent of the bonding in molecules  $\text{F}_2$ ,  $\text{O}_2$ , and  $\text{N}_2$ , for all of which Lewis structures obeying the octet rule can be drawn. The structure of  $\text{TiAl}_3$  raises an issue for future research: when isolobal T–T  $\pi$  bonds will be preferred over adding new T–T contacts to create more  $\sigma$  bonds, a comparison similar to that between the dimeric structure of elemental nitrogen, and the extended structure of phosphorus.

Table 1. Binary Phases Following the 18-*n* Rule in Its Simplest Form

structure type	phase	<i>n</i> <sup>b</sup>	18 - <i>n</i>	VEC <sup>c</sup>	ΔVEC histogram for all phases from ICSD <sup>a</sup>						
					≤-3	-2	-1	0	1	2	≥3
PtHg <sub>4</sub>	CrGa <sub>4</sub> <sup>34</sup>	0	18	18	0	0	0	1	1	0	0
CaF <sub>2</sub>	NiSi <sub>2</sub> <sup>26b</sup>	0	18	18	0	2	5	2	0	0	0
Fe <sub>3</sub> C	IrIn <sub>3</sub> <sup>35</sup>	0	18	18	0	0	0	1	1	0	0
CoGa <sub>3</sub>	FeGa <sub>3</sub> <sup>36</sup>	1	17	17	0	0	1	4	5	0	0
Co <sub>2</sub> Al <sub>5</sub>	Co <sub>2</sub> Al <sub>5</sub> <sup>37</sup>	1.5	16.5	16.5	1	1	0	2	0	0	0
Ru <sub>2</sub> B <sub>3</sub>	Pt <sub>2</sub> Sn <sub>3</sub> <sup>38</sup>	2	16	16	2	0	1	1	0	0	0
β-FeSi <sub>2</sub>	FeSi <sub>2</sub> <sup>39</sup>	2	16	16	0	0	0	2	0	0	0
NiAs	NiAs <sup>40</sup>	3	15	15	16	4	6	15	7	0	0
Ni <sub>2</sub> Al <sub>3</sub>	Ni <sub>2</sub> Al <sub>3</sub> <sup>41</sup>	3	15	14.5	1	0	11 <sup>d</sup>	0	0	0	0
Rh <sub>4</sub> Si <sub>5</sub>	Rh <sub>4</sub> Si <sub>5</sub> <sup>42</sup>	3.5	14.5	14	0	0	2 <sup>d</sup>	0	0	0	0
CrSi <sub>2</sub>	CrSi <sub>2</sub> <sup>43</sup>	4	14	14	0	2	5	1	0	0	0
Ir <sub>3</sub> Ga <sub>5</sub>	Ir <sub>3</sub> Ga <sub>5</sub> <sup>44</sup>	4	14	14	0	0	0	1	0	0	0
Mo <sub>3</sub> Al <sub>8</sub>	Mo <sub>3</sub> Al <sub>8</sub> <sup>45</sup>	4	14	14	0	0	0	1	0	0	0
MnP	PdGe <sup>46</sup>	4	14	14	3	0	7	10	0	0	0
TiSi <sub>2</sub>	RuGa <sub>2</sub> <sup>47</sup>	4	14	14	0	3	1	2	0	0	0
Ru <sub>2</sub> Sn <sub>3</sub>	Ru <sub>2</sub> Sn <sub>3</sub> <sup>48</sup>	4	14	14	0	0	0	1	0	0	0
TiAl <sub>3</sub>	NbAl <sub>3</sub> <sup>49</sup>	4	14	14	0	0	3	6	0	0	0
MoSi <sub>2</sub>	MoSi <sub>2</sub> <sup>50</sup>	4	14	14	0	0	0	7	1	0	0
CoSn	CoSn <sup>51</sup>	4	14	13	0	1	4 <sup>e</sup>	0	0	0	0
ZrAl <sub>3</sub>	ZrAl <sub>3</sub> <sup>49a,52</sup>	5	13	13	0	0	0	3	0	0	0
CsCl	CoAl <sup>53</sup>	6	12	12	3	1	7	14	7	9	0
FeSi	FeSi <sup>54</sup>	6	12	12	2	2	3	6	6	0	0
AuCu <sub>3</sub>	ScAl <sub>3</sub> <sup>55</sup>	6	12	12	0	0	0	5	0	0	1
ZrSi <sub>2</sub>	ZrSi <sub>2</sub> <sup>56</sup>	6	12	12	0	0	3	4	0	0	0
Mn <sub>2</sub> Hg <sub>5</sub>	Mn <sub>2</sub> Hg <sub>5</sub> <sup>57</sup>	6	12	12	0	0	2	1	1	0	2

<sup>a</sup>T-E phases for each structure type are sorted into bins according to the closest integer value for ΔVEC = the experimental VEC minus the 18-*n* prediction. The left- and right-most bins also contain any phases with  $|\Delta\text{VEC}| > 3$ . <sup>b</sup>Average number of electron pairs shared by each T atom with neighboring T atoms. <sup>c</sup>Defined as number of valence electrons per T atom. <sup>d</sup>ΔVEC = -0.5. <sup>e</sup>Electron deficiency accommodated by delocalized  $\pi$  interactions.

Table 2. Binary Intermetallics Following the Generalized 18-*n* + *m* Rule

structure type	phase	<i>n</i> <sup>b</sup>	<i>m</i> <sup>c</sup>	18 - <i>n</i> + <i>m</i>	VEC <sup>d</sup>	ΔVEC histogram for all phases from ICSD <sup>a</sup>						
						≤-3	-2	-1	0	1	2	≥3
FeS <sub>2</sub> (oP6)	NiSb <sub>2</sub> <sup>27b,d</sup>	0	2	20	20	1	7	1	9	4	0	0
	FeSb <sub>2</sub> <sup>27a,c</sup>	2	2	18	18	0	1	0	7	1	9	4
CoAs <sub>3</sub>	CoAs <sub>3</sub> <sup>60</sup>	0	6	24	24	0	0	0	7	0	0	0
	PdSn <sub>2</sub> <sup>26b,61</sup>	1	1	18	18	0	0	1	1	0	0	0
CoSb <sub>2</sub>	CoGe <sub>2</sub> <sup>26b,61</sup>	2	1	17	17	0	0	0	1	1	0	0
	CoSb <sub>2</sub> <sup>27e</sup>	1	2	19	19	0	0	0	23	0	0	0
Ir <sub>3</sub> Ge <sub>7</sub>	Ir <sub>3</sub> Sn <sub>7</sub> <sup>62</sup>	1	1.33	18.33	18.33	0	0	18	4	0	0	0
	Os <sub>3</sub> Sn <sub>7</sub> <sup>63</sup>	2	1.33	17.33	17.33	0	0	0	18	4	0	0
CuAl <sub>2</sub>	CuAl <sub>2</sub> <sup>64</sup>	2 <sup>e</sup>	2	17 <sup>e</sup>	18	7	3	6	2	1	0	0
Re <sub>3</sub> Ge <sub>7</sub>	Re <sub>3</sub> Ge <sub>7</sub> <sup>65</sup>	2.67	1.33	16.67	16.33	0	0	0	1	0	0	0
CrP <sub>2</sub>	OsGe <sub>2</sub> <sup>66</sup>	3	1	16	16	0	0	4	2	0	0	0
Mg <sub>2</sub> Ni	MoSn <sub>2</sub> <sup>67</sup>	6	2 <sup>f</sup>	14	14	0	0	0	2	1	0	0

<sup>a</sup>See footnote a of Table 1. <sup>b</sup>See footnote b of Table 1. <sup>c</sup>The number of electrons per T atom that belong to bonding subsystems orthogonal to the T-centered functions, e.g., E-E bonds. <sup>d</sup>See footnote c of Table 1. <sup>e</sup>See footnote e of Table 1. <sup>f</sup>Half of these Sn-based electrons are delocalized over several contacts in the Sn sublattice, suggesting that *m* in this case is not firmly determined but may depend on the relative electronegativities of the T and E atoms; see the Supporting Information for more details.

## GENERALITY OF THE 18-*n* RULE

In the case studies above, we have shown examples of structural progressions in T-containing intermetallics that can be explained using the 18-*n* bonding scheme. These examples, however, represent only a small number of the T-E intermetallics for which the rule is envisioned. In this section, we evaluate the generality and precision of the 18-*n* rule more broadly by comparing the predicted and observed electron

counts for a wide selection of compounds: 341 phases in 34 binary structure types gleaned from the Inorganic Crystal Structure Database (ICSD).<sup>31</sup>

In Tables 1 and 2, we summarize the data yielded by this survey, sorting the phases according to their values of *n* and *m*. For at least one representative of each structure type, we performed an raMO analysis to demonstrate the importance of 18-electron configurations, and confirm that the correct values

of  $n$  and  $m$  have been assigned in the tables (raMO results for the individual compounds are provided in the *Supporting Information*). The columns  $18-n$  or  $18-n+m$  and valence electron concentration (VEC) provide a comparison of the predicted and observed electron counts for each of the representative phases. To the right of these columns appears a histogram given in table form, in which the relevant phases in the ICSD for each structure type are sorted into bins according to their deviations from the predicted VEC ( $\Delta\text{VEC}$ ), with a bin-width of one electron per T atom. For example, the column  $\text{VEC} = 0$  contains any phase whose VEC deviates from its ideal by less than 0.5 electrons per T ( $|\Delta\text{VEC}| < 0.5$ ).

In Table 1, we list the structure types for which the raMO analysis of the representative phases attributed all electrons to T-centered orbitals. For such cases, the overall valence electron concentration is expected to follow the  $18-n$  count, without the need for additional electrons for separate orbitals based on the E sublattices. The  $n$ -values for this table can be seen to stretch from zero for  $\text{CrGa}_4$ ,  $\text{NiSi}_2$ , and  $\text{IrIn}_3$  all the way to six for  $\text{CoAl}$ ,  $\text{FeSi}$ ,  $\text{ScAl}_3$ ,  $\text{ZrSi}_2$ , and  $\text{Mn}_2\text{Hg}_5$ , suggestive of a wide range of T–T connectivities.

A number of trends can be perceived in the  $\Delta\text{VEC}$  histogram. One is in the variable strictness with which the  $18-n$  rule is followed. Some structure types, particularly those with a small number of members, show tight grouping around  $\Delta\text{VEC} = 0$ . These include  $\beta\text{-FeSi}_2$  and  $\text{ZrAl}_3$ -type phases, as well as the Nowotny Chimney Ladders  $\text{Ru}_2\text{Sn}_3$  and  $\text{Ir}_3\text{Ga}_5$ .

For some others, there are more pronounced ranges of VEC values that stretch more toward the electron-poor side of what is predicted by the  $18-n$  rule. The  $\text{CaF}_2$ -,  $\text{CrSi}_2$ -,  $\text{MnP}$ ,  $\text{TiSi}_2$ -,  $\text{TiAl}_3$ -,  $\text{CoSn}$ -, and  $\text{ZrSi}_2$ -type phases fit into this category. This preference for electron counts below the ideal over ones above it can be simply understood from the nature of the band gap or pseudogap that often accompanies an  $18-n$  VEC. The states just below the gap tend to be T nonbonding orbitals (or perhaps T–T  $\pi^*$  based functions) whose depopulation causes little energetic penalty. The states above the pseudogap, however, are usually there due to their antibonding character. Moving to higher VECs than those given by the  $18-n$  rule would then be expected to provide a stronger driving force for finding structural alternatives. It is thus not surprising that the  $\Delta\text{VEC} = 2$  and  $\geq 3$  columns are largely filled with zeros.

Finally, a handful of structure types exhibit a wide  $\Delta\text{VEC}$  range, seemingly unaware of the benefits of following the  $18-n$  rule. These phases tend to be simple and quite common structures, most notably the  $\text{NiAs}$ ,  $\text{CsCl}$ , and  $\text{FeSi}$  types, where more conventional metallic character might be expected. However, a deeper look into the electronic structures of some of these types shows that the  $18-n$  electron counts can still be associated with stabilizing features. For the  $\text{CsCl}$ -type phase  $\text{CoAl}$ , the Fermi energy lies just at the top of a deep pseudogap. In  $\text{FeSi}$ , however, the Fermi energy coincides with the optimization of Fe–Si interactions as revealed by a crystal orbital Hamilton population analysis (see the *Supporting Information*). The ability of these lattices to endure nonideal VEC values may reflect competing bonding interactions, which serve to reinforce the stability of these simple structures relative to more complex arrangements.<sup>58</sup> For example, the ionic component of the total energy frequently evoked for the  $\text{CsCl}$  type involves long-range electrostatic interactions.<sup>59</sup>

Another feature that can be seen in the histogram of Table 1 is the presence of outliers, as is seen for the  $\text{Ru}_2\text{B}_3$  type. This structure type has two phases at  $\Delta\text{VEC} = 0$  or  $-1$ , with no

entries in the remaining columns except for two more phases in the  $\Delta\text{VEC} \leq -3$  bin. Similar outliers at either end of the histogram also appear for the  $\text{MnP}$  and  $\text{AuCu}_3$  structure types. This concentration of phases around non- $18-n$  electron counts may be indicative of other bonding schemes being satisfied in these cases. For instance, in a traditional Zintl-like scheme, the preferred VEC would be determined by the E–E rather than T–T connectivity.

Thus far, we have considered only T–E phases where raMO analysis shows that the preferred VEC is determined solely by T-centered functions. Let's now turn to binary phases that involve not only filled octadecets on the T atoms but also separate electron pairs in E–E bonds. In Table 2, we summarize our results for a series of such structures we analyzed with the raMO method. A new column for  $m$  is added here, corresponding to the number of valence electrons per T atom that occupy orthogonal E–E bonding functions. The predicted VEC value then becomes generalized to  $18-n+m$ . In Table 2, similar trends to those in Table 1 can be perceived. The  $\Delta\text{VEC}$  histograms exhibit varying degrees of spread but tend to be concentrated either on  $\Delta\text{VEC} = 0$  or  $-1$ .

A new feature for some of these structures, however, is the appearance of multiple possible assignments of  $n$  and  $m$ . In the row for the marcasite ( $\text{FeS}_2$ ,  $o\text{P}6$ )-type phase  $\text{NiSb}_2$  ( $n = 0, m = 2$ ), in particular, two peaks occur, one for seven phases at  $\Delta\text{VEC} = -2$  and one for nine for  $\Delta\text{VEC} = 0$ . If we refer back to our analysis of the marcasite and arsenopyrite phases for case study 2, we arrive at a simple explanation for this bimodal character of the distribution.  $\Delta\text{VEC} = -2$  with reference to  $\text{NiSb}_2$  corresponds to the VEC value of  $\text{FeSb}_2$ , where the shared electron pairs along Fe–Fe contacts bring  $n$  from 0 to 2. Charting  $\Delta\text{VEC}$  values for marcasite-type phases relative to  $\text{FeSb}_2$  (next row in Table 2) then shows a peak of seven phases at  $\Delta\text{VEC} = 0$  and another peak of nine phases at  $\Delta\text{VEC} = 2$ . Similar cleavage or formation of T–T bonds (this time of  $\pi$  character) can account for the  $\Delta\text{VEC}$  range of the  $\text{PdSn}_2$  and  $\text{Ir}_3\text{Ge}_7$  types.

Altogether, Tables 1 and 2 sort over 300 T-based phases according to their adherence to the  $18-n$  rule, allowing us to draw conclusions about the rule's generality. One of the trends to emerge from these tables is not at all surprising: different structures vary in the width of their stability ranges with respect to VEC. For structures with narrow VEC ranges, such as the skutterudite ( $\text{CoAs}_3$ ) or  $\beta\text{-FeSi}_2$  types, the observed VEC values align well with the  $18-n$  prediction. When the VEC distribution for a structure type is a little more broad, the stability range usually appears centered on the  $\Delta\text{VEC} = 0$  bin or the nearest bins to the right or left.

## CONCLUSIONS

In this Article, we have seen how the  $18-n$  rule provides a common language for understanding a range of structural chemistry in transition metal (T)–main group (E) intermetallics. We covered three structural progressions in which changes in the valence electron count lead to structural progressions as isolobal T–T bonds are formed or broken. For the  $\text{NiSi}_2 \rightarrow \beta\text{-FeSi}_2 \rightarrow \text{FeSb}_2 \rightarrow \text{CoSb}_2 \rightarrow \text{NiSb}_2$  sequences, they correspond to small motions of atoms, which lead to superstructures of common basic structures. In the  $\text{ScAl}_3$  to  $\text{ZrAl}_3$  to  $\text{NbAl}_3$  progression, larger-scale changes were encountered, as layers of the structure shift to turn on and off T–T interactions. In these examples, the changes in T–T connectivity were evident not only in the interatomic distances

but also in the raMO functions: T–T isolobal bonds show clear multicenter character involving both T atoms, while at nonbonded T–T contacts the raMOs do not extend appreciably across the pair of T atoms.

To better generalize this picture, we also surveyed a broader range of intermetallic structure types. Here, adherence to the 18-*n* rule for at least one member of each structure type was confirmed using raMO analysis. These confirmed cases were then used as reference points for the creation of histograms of the number of phases adopting these structures as a function of how their valence electron counts deviate from that predicted by the 18-*n* rule. For T–E structure types that are closely associated with a specific electron count, that electron count was found to be well-predicted by the 18-*n* rule.

While these conclusions are drawn from the extensive use of theoretical calculations, one of the advantages of the 18-*n* rule is that it can be applied through geometrical considerations alone. A minimal value for *n* (excluding possible  $\pi$  interactions) can be determined by simply counting the T–T contacts (with E–bridging if the T–T distance exceeds a normal bonding distance). In principle, *m* can be determined by looking for E–E bonding contacts that do not involve interactions with T atoms. This approach should thus be applicable for rationalizing the structures of new T–E compounds even without detailed computational studies, much as the Zintl concept can be applied through counting electrons and bonds. In fact, just as with the Zintl concept, the 18-*n* bonding scheme appears to account for the structures of some experimentally observed phases that exhibit no obvious electronic pseudogaps at their  $E_F$  values.

These criteria can also easily be programmed in software to screen structures for their adherence or nonadherence to the 18-*n* rule. It will be interesting to see whether such a procedure could help identify materials with useful physical properties. Deviations from the 18-*n* rule suggest that the Fermi energy of a system lies away from a band gap or pseudogap, possibly leading to enhanced metallic conductivity, magnetic ordering, or a tendency toward superstructure formation.

While the 18-*n* rule has demonstrated some success for T–E intermetallics, several avenues for future research remain. First, our focus thus far has been on binary intermetallic phases. In our forays into ternary systems, we have found that new challenges arise: the preference for specific electron counts often becomes weaker, which may arise from different interaction types being optimized at different electron counts. Another challenge is how the 18-*n* rule should be generalized in the limits where *n* or *m* become very large. When *n*, the average number of T–T bonds around each T atom, exceeds 9, the T atoms will not have enough valence atomic orbitals to have one orbital for each T–T contact.<sup>68</sup> Instead, T–T clustering will be required in which electron pairs are shared among several T atoms. Such is indeed observed in the electronic structure of Ta<sub>4</sub>Ga<sub>5</sub>.<sup>69</sup> Likewise, large values of *m* can arise from E-rich compositions that allow E atom clusters to develop, such as the Ga@Ga<sub>12</sub> cubooctahedra of V<sub>8</sub>Ga<sub>41</sub><sup>3e</sup> whose preferred electron counts are not obvious. We are looking forward to seeing what new bonding phenomena may be encountered in these systems.

## ASSOCIATED CONTENT

### Supporting Information

The Supporting Information is available free of charge on the ACS Publications website at DOI: [10.1021/acs.inorgchem.5b02016](https://doi.org/10.1021/acs.inorgchem.5b02016).

Detailed computational procedures; optimized geometries and total energies for all intermetallic phases analyzed; tables of DFT-calibrated Hückel parameters used in this work; raMO analyses of CoSi<sub>2</sub>, a hypothetical CaF<sub>2</sub>-type FeSi<sub>2</sub> phase, and intermetallics listed in Tables 1 and 2. ([PDF](#))

## AUTHOR INFORMATION

### Corresponding Author

\*E-mail: [danny@chem.wisc.edu](mailto:danny@chem.wisc.edu).

### Notes

The authors declare no competing financial interest.

## ACKNOWLEDGMENTS

We thank Dr. Veronica Berns, Joshua Engelkemier, Dr. Amelia Hadler, Katerina Hilleke, Yiming Guo, Brandon Kilduff, and Anastasiya Vinokur for their testing of the raMO approach on a variety of systems, many of which have ended up in Tables 1 or 2. In addition, we are grateful to Dr. Rie Fredrickson for her synthetic work in T–E systems, which prompted our interest in the role 18-electron configurations play in these compounds. We also gratefully acknowledge the financial support of the Wisconsin Alumni Research Foundation.

## REFERENCES

- (1) (a) Bergman, G.; Waugh, J. L. T.; Pauling, L. *Acta Crystallogr.* **1957**, *10*, 254–259. (b) Larson, A. C.; Cromer, D. T. *Acta Crystallogr., Sect. B: Struct. Crystallogr. Cryst. Chem.* **1971**, *27*, 1875–1879. (c) Westin, L.; Edshammar, L. E. *Acta Chem. Scand.* **1972**, *26*, 3619–3626. (d) Chabot, B.; Cenzual, K.; Parthé, E. *Acta Crystallogr., Sect. B: Struct. Crystallogr. Cryst. Chem.* **1980**, *36*, 2202–2205. (e) Kuo, K. H. *Struct. Chem.* **2002**, *13*, 221–230. (f) Gómez, C. P.; Lidin, S. *Phys. Rev. B: Condens. Matter Mater. Phys.* **2003**, *68*, 024203.
- (2) (a) Nowotny, H. In *Chemistry of Extended Defects in Nonmetallic Solids*; Eyring, L., O’Keeffe, M., Eds.; North-Holland Publishing Company: Amsterdam, 1970; pp 223–237. (b) Cenzual, K.; Parthé, E.; Waterstrat, R. M. *Acta Crystallogr., Sect. C: Cryst. Struct. Commun.* **1986**, *42*, 261–266. (c) Boström, M.; Lidin, S. *J. Solid State Chem.* **2002**, *166*, 53–57. (d) Stacey, T. E.; Fredrickson, D. C. *Inorg. Chem.* **2013**, *52*, 8349–8359.
- (3) (a) Samson, S. *Nature* **1962**, *195*, 259–262. (b) Samson, S. *Acta Crystallogr.* **1967**, *23*, 586–600. (c) Andersson, S. *Acta Crystallogr., Sect. B: Struct. Crystallogr. Cryst. Chem.* **1980**, *36*, 2513–2516. (d) Yang, Q.-B.; Andersson, S.; Stenberg, L. *Acta Crystallogr., Sect. B: Struct. Sci.* **1987**, *43*, 14–16. (e) Häussermann, U.; Viklund, P.; Svensson, C.; Eriksson, S.; Berastegui, P.; Lidin, S. *Angew. Chem., Int. Ed.* **1999**, *38*, 488–492. (f) Conrad, M.; Harbrecht, B.; Weber, T.; Jung, D. Y.; Steurer, W. *Acta Crystallogr., Sect. B: Struct. Sci.* **2009**, *65*, 318–325. (g) Weber, T.; Dshemuchadse, J.; Kobas, M.; Conrad, M.; Harbrecht, B.; Steurer, W. *Acta Crystallogr., Sect. B: Struct. Sci.* **2009**, *65*, 308–317.
- (4) (a) Lidin, S.; Lind, H.; Eriksson, L.; Larsson, A. K.; Rohrer, F. E. Z. *Kristallogr. - Cryst. Mater.* **2000**, *215*, 650–660. (b) Rohrer, F. E.; Lind, H.; Eriksson, L.; Larsson, A. K.; Lidin, S. Z. *Kristallogr. - Cryst. Mater.* **2001**, *216*, 190–198. (c) Lu, G.; Lee, S.; Lin, J.; You, L.; Sun, J.; Schmidt, J. T. *J. Solid State Chem.* **2002**, *164*, 210–219. (d) Piao, S. Y.; Lidin, S. *Philos. Mag.* **2007**, *87*, 2693–2699. (e) Schmidt, J. T.; Lee, S.; Fredrickson, D. C.; Conrad, M.; Sun, J.; Harbrecht, B. *Chem. - Eur. J.* **2007**, *13*, 1394–1410. (f) Sun, J.; Lee, S.; Lin, J. *Chem. - Asian J.* **2007**, *2*, 1204–1229. (g) Fredrickson, D. C.; Lidin, S.; Venturini, G.; Malaman, B.; Christensen, J. *J. Am. Chem. Soc.* **2008**, *130*, 8195–8214. (h) Lin, Q. S.; Lidin, S.; Corbett, J. D. *Inorg. Chem.* **2008**, *47*, 1020–1029. (i) Lind, H.; Boström, M.; Petříček, V.; Lidin, S. *Acta Crystallogr., Sect. B: Struct. Sci.* **2003**, *59*, 720–729.
- (5) (a) Mott, N. F.; Jones, H. *Theory of the Properties of Metals and Alloys*; Clarendon Press: Oxford, U.K., 1936; (b) Pearson, W. B. *The*

- crystal chemistry and physics of metals and alloys*; Wiley-Interscience: New York, 1972.
- (6) Berger, R. F.; Walters, P. L.; Lee, S.; Hoffmann, R. *Chem. Rev.* **2011**, *111*, 4522–4545.
  - (7) (a) Schäfer, H.; Eisenmann, B.; Müller, W. *Angew. Chem., Int. Ed. Engl.* **1973**, *12*, 694–712. (b) *Chemistry, structure, and bonding of Zintl phases and ions*; Kauzlarich, S. M., Ed.; VCH: New York, 1996.
  - (8) Shevelkov, A. V.; Shatruk, M. M. *Russ. Chem. Bull.* **2001**, *50*, 337–352.
  - (9) (a) Belin, C.; Tillard-Charbonnel, M. *Prog. Solid State Chem.* **1993**, *22*, 59–109. (b) Fässler, T. F.; Kronseder, C. *Angew. Chem., Int. Ed. Engl.* **1997**, *36*, 2683–2686. (c) Xu, Z.; Guloy, A. M. *J. Am. Chem. Soc.* **1997**, *119*, 10541–10542. (d) Goodey, J.; Mao, J.; Guloy, A. M. *J. Am. Chem. Soc.* **2000**, *122*, 10478–10479. (e) Mills, A. M.; Lam, R.; Ferguson, M. J.; Deakin, L.; Mar, A. *Coord. Chem. Rev.* **2002**, *233*–234, 207–222. (f) Amerioun, S.; Häussermann, U. *Inorg. Chem.* **2003**, *42*, 7782–7788. (g) Lee, C.-S.; Miller, G. J. *J. Solid State Chem.* **2003**, *170*, 94–105. (h) Mao, J.-G.; Goodey, J.; Guloy, A. M. *Inorg. Chem.* **2004**, *43*, 282–289. (i) Lupu, C.; Downie, C.; Guloy, A. M.; Albright, T. A.; Mao, J.-G. *J. Am. Chem. Soc.* **2004**, *126*, 4386–4397. (j) Guttsche, K.; Rosin, A.; Wendorff, M.; Röhr, C. Z. *Naturforsch., B: J. Chem. Sci.* **2006**, *61*, 846–853. (k) Köhler, J.; Whangbo, M.-H. *Chem. Mater.* **2008**, *20*, 2751–2756. (l) Corbett, J. D. *Inorg. Chem.* **2010**, *49*, 13–28. (m) Slabon, A.; Cuervo-Reyes, E.; Kubata, C.; Mensing, C.; Nesper, R. Z. *Anorg. Allg. Chem.* **2012**, *638*, 2020–2028. (n) Xu, Z.; Guloy, A. M. *J. Am. Chem. Soc.* **1998**, *120*, 7349–7350. (o) You, T.-S.; Tobash, P. H.; Bobev, S. *Inorg. Chem.* **2010**, *49*, 1773–1783.
  - (10) (a) Xu, J.-h.; Freeman, A. J. *Phys. Rev. B: Condens. Matter Mater. Phys.* **1989**, *40*, 11927–11930. (b) Boyen, H.-G.; Indlekofer, G.; Oelhafen, P.; Häussler, P.; Baumann, F.; Moruzzi, V. L. *Mater. Sci. Eng., A* **1991**, *133*, 107–110. (c) Ravindran, P.; Subramonian, G.; Asokamani, R. *Phys. Rev. B: Condens. Matter Mater. Phys.* **1996**, *53*, 1129–1137. (d) Tobola, J.; Pierre, J.; Kaprzyk, S.; Skolozdra, R. V.; Kouacou, M. A. *J. Magn. Magn. Mater.* **1996**, *159*, 192–200. (e) Wolf, W.; Bihlmayer, G.; Blügel, S. *Phys. Rev. B: Condens. Matter Mater. Phys.* **1997**, *55*, 6918–6926. (f) Tobola, J.; Pierre, J.; Kaprzyk, S.; Skolozdra, R. V.; Kouacou, M. A. *J. Phys.: Condens. Matter* **1998**, *10*, 1013–1032. (g) Imai, Y.; Mukaida, M.; Tsunoda, T. *Intermetallics* **2000**, *8*, 381–390. (h) Jung, D.; Koo, H. J.; Whangbo, M. H. *J. Mol. Struct.: THEOCHEM* **2000**, *527*, 113–119. (i) Tobola, J.; Pierre, J. *J. Alloys Compd.* **2000**, *296*, 243–252. (j) Colinet, C.; Pasturel, A. *Phys. Rev. B: Condens. Matter Mater. Phys.* **2001**, *64*, 205102. (k) Häussermann, U.; Viklund, P.; Boström, M.; Norrestam, R.; Simak, S. *Phys. Rev. B: Condens. Matter Mater. Phys.* **2001**, *63*, 125118. (l) Vajeeston, P.; Ravindran, P.; Ravi, C.; Asokamani, R. *Phys. Rev. B: Condens. Matter Mater. Phys.* **2001**, *63*, 045115. (m) Imai, Y.; Watanabe, A. *J. Alloys Compd.* **2006**, *417*, 173–179. (n) Kandpal, H. C.; Felser, C.; Seshadri, R. *J. Phys. D: Appl. Phys.* **2006**, *39*, 776–785. (o) Chen, Z.; Zou, H.; Yu, F.; Zou, J. *J. Phys. Chem. Solids* **2010**, *71*, 946–951. (p) Krüger, E. *J. Supercond. Novel Magn.* **2010**, *23*, 213–223. (q) Berns, V. M.; Stacey, T. E.; Sapiro, M.; Fredrickson, D. C. *Eur. J. Inorg. Chem.* **2011**, *2011*, 3936–3949. (r) Blankenship, T. V.; Lita, A.; Lattner, S. E. *Inorg. Chem.* **2012**, *51*, 13345–13350. (s) Smetana, V.; Miller, G. J.; Corbett, J. D. *Inorg. Chem.* **2012**, *51*, 7711–7721.
  - (11) Fredrickson, R. T.; Fredrickson, D. C. *Inorg. Chem.* **2012**, *51*, 10341–10349.
  - (12) Fredrickson, R. T.; Fredrickson, D. C. *Inorg. Chem.* **2013**, *52*, 3178–3189.
  - (13) Yannello, V. J.; Kilduff, B. J.; Fredrickson, D. C. *Inorg. Chem.* **2014**, *53*, 2730–2741.
  - (14) (a) Hadler, A. B.; Fredrickson, D. C. *J. Am. Chem. Soc.* **2012**, *134*, 10361–10364. (b) Hadler, A. B.; Yannello, V. J.; Bi, W.; Alp, E. E.; Fredrickson, D. C. *J. Am. Chem. Soc.* **2014**, *136*, 12073–12084.
  - (15) Yannello, V. J.; Fredrickson, D. C. *Inorg. Chem.* **2014**, *53*, 10627–10631.
  - (16) (a) Kresse, G.; Furthmüller, J. *Phys. Rev. B: Condens. Matter Mater. Phys.* **1996**, *54*, 11169–11186. (b) Kresse, G.; Furthmüller, J. *Comput. Mater. Sci.* **1996**, *6*, 15–50.
  - (17) (a) Blöchl, P. E. *Phys. Rev. B: Condens. Matter Mater. Phys.* **1994**, *50*, 17953–17979. (b) Kresse, G.; Joubert, D. *Phys. Rev. B: Condens. Matter Mater. Phys.* **1999**, *59*, 1758–1775.
  - (18) Stacey, T. E.; Fredrickson, D. C. *Dalton Trans.* **2012**, *41*, 7801–7813.
  - (19) Landrum, G. A.; Glassey, W. V. YAeHMOP: Yet Another extended Huckel Molecular Orbital Program, Version 3.0. YAeHMOP is freely available via the WWW at URL <http://yaehmop.sourceforge.net/>.
  - (20) Hoffmann, R. *Angew. Chem., Int. Ed. Engl.* **1982**, *21*, 711–724.
  - (21) Beyond the examples discussed in this Article, the isolobal T–T bond concept can also be used to interpret (a) the four-center four-electron bonds in the  $Zn_2Sb_2$  clusters of 1:1 and 4:3 zinc antimonides: Mikhaylushkin, A. S.; Nylen, J.; Häussermann, U. *Chem. - Eur. J.* **2005**, *11*, 4912–4920. and (b) electron localization along the Al-bridged Ir–Au contacts of  $Al_3AuIr$ : Kadok, J.; de Weerd, M.-C.; Boulet, P.; Gaudry, É.; Grin, Y.; Fournée, V.; Ledieu, J. *Inorg. Chem.* **2015**, *54*, 7898–7905.
  - (22) (a) Nagai, H. *Mater. Trans., JIM* **1995**, *36*, 365–372. (b) Pandey, T.; Singh, D. J.; Parker, D.; Singh, A. K. *J. Appl. Phys.* **2013**, *114*, 153704. (c) Fedorov, M. I.; Isachenko, G. N. *Jpn. J. Appl. Phys.* **2015**, *54*, 07JA05.
  - (23) Further technical details underlying the raMO approach, as well as comparisons with Wannier function method and natural bond orbital analysis, are given in ref 13.
  - (24) (a) Birkholz, U.; Schelm, J. *Phys. Status Solidi B* **1968**, *27*, 413–425. (b) Giannini, C.; Lagomarsino, S.; Scarinci, F.; Castrucci, P. *Phys. Rev. B: Condens. Matter Mater. Phys.* **1992**, *45*, 8822–8824.
  - (25) (a) Pan, Z. J.; Zhang, L. T.; Wu, J. S. *Mater. Sci. Eng., B* **2006**, *131*, 121–126. (b) Opahle, I.; Parma, A.; McEniry, E. J.; Drautz, R.; Madsen, G. K. H. *New J. Phys.* **2013**, *15*, 105010.
  - (26) (a) Bertaut, F.; Blum, P. C. R. *Hebd. Séances Acad. Sci.* **1950**, *231*, 626–628. (b) Schubert, K.; Pfisterer, H. Z. *Metallkd.* **1950**, *41*, 433–441. (c) Wittmann, A.; Burger, K. O.; Nowotny, H. *Monatsh. Chem.* **1961**, *92*, 961–966. (d) Krendelsberger, N.; Weitzer, F.; Schuster, J. C.; Stein, F. *Intermetallics* **2013**, *38*, 92–101.
  - (27) (a) Hägg, G. Z. *Kristallogr. Kristallgeom. Kristallphys. Kristallchem.* **1928**, *68*, 470–472. (b) Rosenqvist, T. *Acta Crystallogr.* **1954**, *7*, 636. (c) Holseth, H.; Kjekshus, A. *Acta Chem. Scand.* **1969**, *23*, 3043–3050. (d) Kjekshus, A.; Rakke, T.; Andresen, A. F. *Acta Chem. Scand.* **1974**, *A28*, 996–1000. (e) Siegrist, T.; Hulliger, F. J. *Solid State Chem.* **1986**, *63*, 23–30.
  - (28) Canadell, E.; Whangbo, M. H. *Chem. Rev.* **1991**, *91*, 965–1034.
  - (29) (a) Diakhate, M. S.; Hermann, R. P.; Mochel, A.; Sergueev, I.; Sondergaard, M.; Christensen, M.; Verstraete, M. J. *Phys. Rev. B: Condens. Matter Mater. Phys.* **2011**, *84*, 125210. (b) Lazarević, N.; Radonjić, M. M.; Tanasković, D.; Hu, R.; Petrović, C.; Popović, Z. V. J. *Phys.: Condens. Matter* **2012**, *24*, 255402. (c) Bachhuber, F.; Rothbäcker, J.; Söhnle, T.; Weihrich, R. *J. Chem. Phys.* **2013**, *139*, 214705. (d) Brahmia, M.; Bennecer, B.; Hamidani, A. *Mater. Sci. Eng., B* **2013**, *178*, 1249–1256. (e) Liao, B.; Lee, S.; Esfarjani, K.; Chen, G. *Phys. Rev. B: Condens. Matter Mater. Phys.* **2014**, *89*, 035108. (f) Luo, X.-N.; Dong, C.; Liu, S.-K.; Zhang, Z.-P.; Li, A.-L.; Yang, L.-H.; Li, X.-C. *Chin. Phys. B* **2015**, *24*, 067201.
  - (30) (a) Hulliger, F.; Mooser, E. *J. Phys. Chem. Solids* **1965**, *26*, 429–433. (b) Brostigen, G.; Kjekshus, A. *Acta Chem. Scand.* **1970**, *24*, 2983–2992. (c) Goodenough, J. B. *J. Solid State Chem.* **1972**, *5*, 144–152. (d) Petrović, C.; Kim, J. W.; Bud'ko, S. L.; Goldman, A. I.; Canfield, P. C.; Choe, W.; Miller, G. J. *Phys. Rev. B: Condens. Matter Mater. Phys.* **2003**, *67*, 155205. (e) Petrović, C.; Lee, Y.; Vogt, T.; Lazarov, N. D.; Bud'ko, S. L.; Canfield, P. C. *Phys. Rev. B: Condens. Matter Mater. Phys.* **2005**, *72*, 045103. (f) Sun, P.; Oeschler, N.; Johnsen, S.; Iversen, B. B.; Steglich, F. *Dalton Trans.* **2010**, *39*, 1012–1019. (g) Bugaris, D. E.; Malliakas, C. D.; Shoemaker, D. P.; Do, D. T.; Chung, D. Y.; Mahanti, S. D.; Kanatzidis, M. G. *Inorg. Chem.* **2014**, *53*, 9959–9968.
  - (31) (a) Bergerhoff, G.; Hundt, R.; Sievers, R.; Brown, I. D. *J. Chem. Inf. Model.* **1983**, *23*, 66–69. (b) Bergerhoff, G.; Brown, I. D. In *Crystallographic Databases*; Allen, F. H.; Bergerhoff, G.; Sievers, R.,

- Eds.; International Union of Crystallography: Chester, 1987; p 77–95. (c) Belsky, A.; Hellenbrandt, M.; Karen, V. L.; Luksch, P. *Acta Crystallogr., Sect. B: Struct. Sci.* **2002**, *58*, 364–369.
- (32) (a) Hong, T.; Watson-Yang, T. J.; Freeman, A. J.; Oguchi, T.; Xu, J. *Phys. Rev. B: Condens. Matter Mater. Phys.* **1990**, *41*, 12462–12467. (b) Xu, J.; Freeman, A. J. *Phys. Rev. B: Condens. Matter Mater. Phys.* **1990**, *41*, 12553–12561. (c) Xu, J.; Freeman, A. J. *J. Mater. Res.* **1991**, *6*, 1188–1199. (d) Vajenine, G. V.; Hoffmann, R. *J. Am. Chem. Soc.* **1998**, *120*, 4200–4208. (e) Condron, C. L.; Miller, G. J.; Strand, J. D.; Bud'ko, S. L.; Canfield, P. C. *Inorg. Chem.* **2003**, *42*, 8371–8376.
- (33) We reached the same conclusion for TiAl<sub>3</sub>-type transition metal gallides in Kilduff, B. J.; Yannello, V. J.; Fredrickson, D. C. *Inorg. Chem.* **2015**, *54*, 8103–8110.
- (34) Meissner, H.-G.; Schubert, K. Z. *Metallkd.* **1965**, *56*, 523–530.
- (35) Flandorfer, H. *J. Alloys Compd.* **2004**, *368*, 256–259.
- (36) (a) Schubert, K.; Breimer, H.; Gohle, R.; Lukas, H. L.; Meissner, H. G.; Stoltz, E. *Naturwissenschaften* **1958**, *45*, 360–361. (b) Häussermann, U.; Boström, M.; Viklund, P.; Rapp, Ö.; Björnängen, T. *J. Solid State Chem.* **2002**, *165*, 94–99.
- (37) (a) Bradley, A. J.; Cheng, C. S. Z. *Kristallogr. - Cryst. Mater.* **1938**, *99*, 480–487. (b) Burkhardt, U.; Ellner, M.; Grin, Y.; Baumgartner, B. *Powder Diffr.* **1998**, *13*, 159–162.
- (38) Schubert, K.; Pfisterer, H. Z. *Metallkd.* **1949**, *40*, 405–411.
- (39) (a) Wandji, R.; Dusausoy, Y.; Protas, J.; Roques, B. *C. R. Acad. Sci., Paris, Ser. C* **1968**, *267*, 1587–1590. (b) Dusausoy, Y.; Protas, J.; Wandji, R.; Roques, B. *Acta Crystallogr., Sect. B: Struct. Crystallogr. Cryst. Chem.* **1971**, *27*, 1209–1218.
- (40) Alsen, N. *Geol. Foeren. Stockholm Foerh.* **1925**, *47*, 19–72.
- (41) Bradley, A. J.; Taylor, A. *London Edinburgh Dublin Philos. Mag. J. Sci.* **1937**, *23*, 1049–1067.
- (42) Engstrom, I. *Acta Chem. Scand.* **1968**, *22*, 3127–3136.
- (43) (a) Borén, B. *Arkiv. Kemi, Mineral. Geol.* **1933**, *11A*, 1–28. (b) Dasgupta, T.; Etourneau, J.; Chevalier, B.; Matar, S. F.; Umarji, A. M. *J. Appl. Phys.* **2008**, *103*, 113516.
- (44) Völlenkle, H.; Wittmann, A.; Nowotny, H. *Monatsh. Chem.* **1967**, *98*, 176–183.
- (45) Forsyth, J. B.; Gran, G. *Acta Crystallogr.* **1962**, *15*, 100–104.
- (46) Pfisterer, H.; Schubert, K. Z. *Metallkd.* **1950**, *41*, 358–367.
- (47) Jeitschko, W.; Holleck, H.; Nowotny, H.; Benesovsky, F. *Monatsh. Chem.* **1963**, *94*, 838–840.
- (48) Schwomma, O.; Nowotny, H.; Wittmann, A. *Monatsh. Chem.* **1964**, *95*, 1538–1543.
- (49) (a) Brauer, G. Z. *Anorg. Allg. Chem.* **1939**, *242*, 1–22. (b) Lundin, C. E.; Yamamoto, A. S. *Trans. Metall. Soc. AIME* **1966**, *236*, 863–872.
- (50) Zachariasen, W. H. Z. *Phys. Chem.* **1927**, *128*, 39–48.
- (51) (a) Nial, O. Z. *Anorg. Allg. Chem.* **1938**, *238*, 287–296. (b) Larsson, A. K.; Haeberlein, M.; Lidin, S.; Schwarz, U. *J. Alloys Compd.* **1996**, *240*, 79–84.
- (52) Ma, Y.; Romming, C.; Lebech, B.; Gjønnes, J.; Taftø, J. *Acta Crystallogr., Sect. B: Struct. Sci.* **1992**, *48*, 11–16.
- (53) (a) Bradley, A. J.; Seager, G. C. *J. Inst. Met.* **1939**, *64*, 81–91. (b) Dutchak, Y. I.; Chekh, V. G. *Zh. Fiz. Khim.* **1981**, *55*, 2342–2345.
- (54) (a) Wever, F.; Möller, H. Z. *Kristallogr. Kristallgeom. Kristallphys. Kristallchem.* **1930**, *75*, 362–365. (b) Sales, B. C.; Jones, E. C.; Chakoumakos, B. C.; Fernandez-Baca, J. A.; Harmon, H. E.; Sharp, J. W.; Volckmann, E. H. *Phys. Rev. B: Condens. Matter Mater. Phys.* **1994**, *50*, 8207–8213.
- (55) (a) Rechkin, V. N.; Lamikhov, L. K.; Samsonova, T. I. *Kristallografiya* **1964**, *9*, 405–408. (b) Zalutskii, I. I.; Kripyakevich, P. I. *Kristallografiya* **1967**, *12*, 394–397.
- (56) (a) Schachner, H.; Nowotny, H.; Kudielka, H. *Monatsh. Chem.* **1954**, *85*, 1140–1153. (b) Zatorska, G. M.; Dmytriv, G. S.; Pavlyuk, V. V.; Bartoszak-Adamska, E.; Jaskólski, M. *J. Alloys Compd.* **2002**, *346*, 154–157.
- (57) de Wet, J. F. *Acta Crystallogr.* **1961**, *14*, 733–738.
- (58) Similar synergistic effects induced by symmetry were found to obscure the role of dipole–dipole interactions in shaping the crystal structures of organic molecules. See: Lee, S.; Mallik, A. B.; Fredrickson, D. C. *Cryst. Growth Des.* **2004**, *4*, 279–290.
- (59) Todorov, E.; Evans, M.; Lee, S.; Rousseau, R. *Chem. - Eur. J.* **2001**, *7*, 2652–2662.
- (60) (a) Oftedal, I. Z. *Kristallogr. - Cryst. Mater.* **1928**, *66*, 517–546. (b) Mandel, N.; Donohue, J. *Acta Crystallogr., Sect. B: Struct. Crystallogr. Cryst. Chem.* **1971**, *27*, 2288–2289.
- (61) Hellner, E. Z. *Kristallogr. Kristallgeom. Kristallphys. Kristallchem.* **1956**, *107*, 99–123.
- (62) (a) Nowotny, H.; Schubert, K.; Dettinger, U. *Metallforschung* **1946**, *1*, 137–145. (b) Schlüter, M.; Häussermann, U.; Heying, B.; Pöttgen, R. *J. Solid State Chem.* **2003**, *173*, 418–424.
- (63) (a) Kalyaeva, N. V.; Popova, S. V. *Izv. Akad. Nauk SSSR, Neorg. Mater.* **1983**, *19*, 1106–1109. (b) Künnen, B.; Niepmann, D.; Jeitschko, W. *J. Alloys Compd.* **2000**, *309*, 1–9.
- (64) (a) Bradley, A. J.; Jones, P. *J. Inst. Met.* **1933**, *51*, 131–162. (b) Meetsma, A.; De Boer, J. L.; Van Smaalen, S. *J. Solid State Chem.* **1989**, *83*, 370–372.
- (65) Siegrist, T.; Hulliger, F.; Petter, W. *J. Less-Common Met.* **1983**, *90*, 143–151.
- (66) Weitz, G.; Born, L.; Hellner, E. Z. *Metallkd.* **1960**, *51*, 238–243.
- (67) Wölpl, T.; Jeitschko, W. Z. *Anorg. Allg. Chem.* **1994**, *620*, 467–470.
- (68) In practice, the localization of functions along individual T–T contacts becomes difficult beyond  $n = 6$ .
- (69) Fredrickson, R. T.; Kilduff, B. J.; Fredrickson, D. C. *Inorg. Chem.* **2015**, *54*, 821–831.